EVANESCENT FIELD EXPOSED MICROSTRUCTURE FIBERS FOR OPTICAL SENSING

NG WEE LIT

FACULTY OF ENGINEERING
UNIVERSITY OF MALAYA
KUALA LUMPUR

2018

EVANESCENT FIELD EXPOSED MICROSTRUCTURE FIBERS FOR OPTICAL SENSING

NG WEE LIT

THESIS SUBMITTED IN FULFILMENT OF THE REQUIREMENTS FOR THE DEGREE OF DOCTOR OF PHILOSOPHY

FACULTY OF ENGINEERING
UNIVERSITY OF MALAYA
KUALA LUMPUR

2018

UNIVERSITY OF MALAYA

ORIGINAL LITERARY WORK DECLARATION

Name of Candidate: **Ng Wee Lit**

Matric No: **KHA130079**

Name of Degree: **Doctor of Philosophy**

Title of ~~Project Paper~~/~~Research Report~~/~~Dissertation~~/Thesis ("this Work"):

Evanescent Field Exposed Microstructure Fibers for Optical Sensing

Field of Study: **Photonics**

I do solemnly and sincerely declare that:

(1) I am the sole author/writer of this Work;
(2) This Work is original;
(3) Any use of any work in which copyright exists was done by way of fair dealing and for permitted purposes and any excerpt or extract from, or reference to or reproduction of any copyright work has been disclosed expressly and sufficiently and the title of the Work and its authorship have been acknowledged in this Work;
(4) I do not have any actual knowledge nor do I ought reasonably to know that the making of this work constitutes an infringement of any copyright work;
(5) I hereby assign all and every rights in the copyright to this Work to the University of Malaya ("UM"), who henceforth shall be owner of the copyright in this Work and that any reproduction or use in any form or by any means whatsoever is prohibited without the written consent of UM having been first had and obtained;
(6) I am fully aware that if in the course of making this Work I have infringed any copyright whether intentionally or otherwise, I may be subject to legal action or any other action as may be determined by UM.

Candidate's Signature Date:

Subscribed and solemnly declared before,

Witness's Signature Date:

Name:

Designation:

EVANESCENT FIELD EXPOSED MICROSTRUCTURE FIBERS FOR OPTICAL SENSING

ABSTRACT

In this work, a modified photonic crystal fiber (PCF) that we refer to as Sunny PCF is proposed. The Sunny PCF with triangular interstitial air holes surrounding the core region increases the interaction of guided modes with the surrounding media. Full-vectorial finite element method (FEM) with perfectly matched layer boundary condition is used to design and simulate the evanescent field exposure and confinement loss characteristics of the proposed Sunny PCF. By adding sunny structure to a conventional PCF with air-filling ratio of 0.9, the highest achievable evanescent field exposure with negligible confinement loss can be significantly increased to 21.23% from 15.83% (for a comparative non-Sunny PCF) at the operating wavelength of 1550 nm. A preliminary Sunny PCF has been fabricated to prove the feasibility of the proposed structure. In the second part of this work, a new microstructured optical fiber (MOF) which can provide large cavities besides high evanescent field exposure and low confinement loss has been proposed, named Diamond Ring Fiber (DRF). Large cavities ease the infiltration of analyte and allow material coating for certain sensing applications. A silica core is supported by a thin ring in the middle of DRF, forming two large air holes in this fiber. Silica core surrounded by air allows high exposure of guided mode into the air with low confinement loss. 3 DRFs with different parameters have been fabricated using stack and draw method. An experiment has been carried out to study the beam profile of guided mode in different sizes of DRFs. Full-vectorial FEM with perfectly matched layer boundary condition is used to simulate the performance of the fibers using Scanning Electron Microscope (SEM) cross sectional images obtained. DRF with the core size of 0.8 μm can achieve high evanescent field exposure of 39.56% with low confinement loss

of 0.027 dB/m at the wavelength of 1550 nm while providing two large cavities with the diameter of 4.2 μm and 10.8 μm respectively. This work is part of a larger effort in using surface plasmon resonance (SPR) for biosensing where the long term target is to adopt fiber technologies as a substrate as opposed to silicon based fabrication. A highly sensitive DRF based SPR sensor for refractive index sensing is then simulated. Chemically-active plasmonic material (gold) layer is coated inside the large cavity of DRF, and the analyte is infiltrated directly through the fiber. The light guiding properties and sensing performances are numerically investigated using FEM. The proposed sensor shows a maximum wavelength and amplitude interrogation sensitivity of 6,000 nm/RIU and 508 RIU^{-1}, respectively over the refractive index range of 1.33-1.39. Additionally, it also shows a sensor resolution of 1.67×10^{-5} RIU and 1.97×10^{-5} RIU by following the wavelength and amplitude interrogation methods, respectively.

Keywords: Evanescent field exposure; confinement loss; simulation; fabrication; surface plasmon resonance

EVANESCENT FIELD EXPOSED MICROSTRUCTURE FIBERS FOR OPTICAL SENSING

ABSTRAK

Dalam kajian ini, satu gentian kristal fotonik (PCF) diubahsuai yang kami rujuk sebagai *Sunny* PCF telah dicadangkan untuk mendedahkan lebih banyak *evanescent field*. *Sunny* PCF mengandungi lubang udara celahan segi tiga sekitar kawasan teras yang dapat meningkatkan interaksi mod dipandu dengan sekeliling. *Full-vectorial finite element* (FEM) bersama dengan keadaan sempadan yang dilapiskan *perfectly matched layer* digunakan untuk mereka bentuk dan menjalankan simulasi terhadap kadar pendedahan *evanescent field* dan kehilangan kurungan di dalam *Sunny* PCF. Dengan menambah struktur celahan kepada PCF konvensional dengan nisbah udara-pengisian 0.9, pendedahan tertinggi dengan kehilangan kurungan yang boleh diabaikan telahpun ditingkatkan ke 21.23% dari 15.83% dengan ketara (berbanding dengan PCF yang tidak ber-*Sunny*) pada panjang gelombang operasi 1550 nm. *Sunny* PCF peringkat awal telah dihasilkan untuk membuktikan kemungkinan struktur yang dicadangkan. Dalam bahagian kedua kajian ini, satu gentian optik mikrostruktur (MOF) baru yang dapat menawar lubang udara besar selain daripada pendedahan *evanescent field* yang tinggi dan kehilangan kurungan yang rendah telah dicadangkan, dinamakan gentian cincin berlian (DRF). Rongga besar memudahkan penyusupan analit dan membolehkan bahan salutan untuk aplikasi penderiaan tertentu. Satu teras silika disokong oleh cincin nipis di pertengahan DRF, membentuk dua lubang udara yang besar dengan gentian ini. Teras silika dikelilingi oleh udara membolehkan pendedahan mod dipandu yang tinggi ke udara dengan kehilangan kurungan rendah. 3 DRF dengan parameter yang berbeza telah dihasilkan menggunakan kaedah timbun dan tarik. Satu eksperimen telah dijalankan untuk mengkaji profil mod dipandu dalam DRF yang berlainan saiz. FEM bersama dengan keadaan sempadan yang dilapiskan *perfectly matched layer* digunakan untuk

menjalankan simulasi ke atas prestasi DRF berasaskan imej-imej mikroskop imbasan elektron (SEM) pada bahagian silang. DRF dengan saiz teras 0.8 μm boleh mencapai pendedahan *evanescent field* setinggi 39.56% dengan kehilangan kurungan yang rendah 0.027 dB/m pada panjang gelombang operasi 1550 nm disamping menyediakan dua rongga besar yang berukuran 4.2 μm dan 10.8 μm. Kerja ini adalah sebahagian daripada usaha yang lebih besar dalam menggunakan resonans plasmon permukaan (SPR) untuk biosensing di mana sasaran jangka panjang adalah untuk mengadopsi teknologi serat sebagai substrat yang bertentangan dengan fabrikasi berasaskan silicon. Satu sensor indeks biasan berasas SPR telah dicadangkan dengan menggunakan DRF. Lapisan bahan plasmonik (emas) yang aktif secara kimia disalutkan di dalam rongga besar DRF, dan analit dibiar menyusup terus melalui rongga DRF. Ciri-ciri membimbing cahaya dan prestasi penginderaan telah disiasat secara berangka menggunakan FEM. Sensor yang dicadangkan menunjukkan sensitiviti pengukuran panjang gelombang dan amplitud setinggi 6,000 nm/RIU dan 508 RIU^{-1}, masing-masing dalam rentang indeks bias 1.33-1.39. Di samping itu, ia juga menunjukkan resolusi sensor 1.67×10^{-5} RIU dan 1.97×10^{-5} RIU dengan mengikuti kaedah pengukuran panjang gelombang dan amplitud.

Kata kunci: Kadar pendedahan *evanescent field*; kehilangan kurungan; simulasi; fabrikasi; resonans plasmon permukaan

ACKNOWLEDGEMENTS

I would like to express my appreciation to the following people who supported me throughout this thesis:

My supervisor, Professor Dr Faisal Rafiq Mahamd Adikan from the University of Malaya, for his guidance and encouragements throughout my study. I am especially grateful with the opportunities given including participation in local and international conferences and research placement.

Every member and alumni of the Integrated Lightwave Research Group, University of Malaya, for the technical and moral support. Special thanks to Dr Ghafour Amouzad Mahdiraji for his supervision on operating the fiber draw tower, Dr Tee Din Chai for his advice on doing numerical analysis, Dr Shee Yu Gang and Dr Wong Wei Ru for their sharing on writing high impact journal papers.

My wife, for accompanying me through the hardships. My parents, for their support and encouragements. Without them, there is no me.

TABLE OF CONTENTS

LIST OF FIGURES

LIST OF TABLES

LIST OF SYMBOLS AND ABBREVIATIONS

n_1	:	Higher refractive index
n_2	:	Lower refractive index
Θ_i	:	Angle of incidence
Θ_r	:	Angle of reflection
Θ_t	:	Angle of transmission
$E^{\parallel}$	:	Electric field vector parallel to the plane of incidence
$E^{\perp}$	:	Electric field vector perpendicular to the plane of incidence
P	:	Phase factor of the transmitted wave
$\mathbf{k_t}$	:	Wave vector associated with the transmitted wave
λ_0	:	Wavelength of radiation in vacuum
F(y)	:	Decay with distance in the second medium
ρ_0	:	Initial diameter of fiber
ρ	:	Final diameter of tapered fiber/Distance from the beginning of the PML
L_0	:	Stretching length
Z	:	Elongation distance
d	:	Air hole diameter/Outer diameter of capillary in DRF preform
Λ	:	Pitch size
d/Λ	:	Air filling ratio
f	:	Evanescent field exposure
Im[n_{eff}]	:	Imaginary part of the effective refractive index
λ	:	Operating wavelength
d_{defect}	:	Air hole diameter at the middle of the silica core
E	:	Electric field intensity

$\mathbf{H}$	:	Magnetic field intensity
$\mathbf{D}$	:	Electric flux density
$\mathbf{B}$	:	Magnetic flux density
ε_0	:	Free space's permittivity
μ_0	:	Free space's permeability
c	:	Speed of light in free space
$\varepsilon(r)$	:	Relative permittivity
$\mu(r)$	:	Relative permeability
n	:	Refractive index
ω	:	Angular frequency
β	:	Propagation constant along the *z*-direction
ω_j	:	Resonant frequencies
B_j	:	Strength of the resonances
s_x	:	PML parameters
s_y	:	PML parameters
d_i	:	PML width in the horizontal or vertical direction
b	:	PML free-parameter
a_{max}	:	PML free-parameter
α	:	PML free-parameter/Confinement loss
n_{eff}	:	Effective refractive index
Re[n_{eff}]	:	Real part of the effective refractive index
A_f	:	Cross-sectional area of preform
A_d	:	Cross-sectional area of capillary
v_f	:	Feeding speed

v_d	:	Drawing speed
$h_1(z)$	:	Physical dimension of preform
$h_2(z)$	:	Physical dimension of preform
$h_1(0)$	:	Dimension of the preform tube
$h_2(0)$	:	Dimension of the preform tube
L	:	Furnace's hot zone length
γ	:	Surface tension coefficient
C	:	Extend of capillary collapse
μ	:	Viscosity
D	:	Inner diameter of the jacket glass tube
d_{core}	:	Diameter of the core
d_1	:	Inner diameter of the ring
d_2	:	Inner diameter of the shield
t_r	:	Thickness of the ring
t_{gold}	:	Thickness of gold metal layer
n_{silica}	:	Refractive index of silica
ε_{Au}	:	Permittivity of the gold material
ε_∞	:	Permittivity at high frequency
ω_D	:	Plasma frequency
γ_D	:	Damping frequency
$\Delta\varepsilon$	:	Weighting factor
n_a	:	Refractive index of analyte
$S_\lambda(\lambda)$	:	Wavelength interrogation sensitivity
$\Delta\lambda_{peak}$	:	Peak shift

$S_A(\lambda)$	:	Amplitude interrogation sensitivity
MOF	:	Microstructured Optical Fiber
PCF	:	Photonic Crystal Fiber
SPR	:	Surface Plasmon Resonance
DRF	:	Diamond Ring Fiber
SMTF	:	Single-mode Tapered Fiber
PBGF	:	Photonic Bandgap Fiber
SMF	:	Single Mode Fiber
MM	:	Multipole Method
PWEM	:	Plane Wave Expansion Method
EME	:	Eigenmode Expansion Method
FEM	:	Finite Element Method
PDE	:	Partial Differential Equation
PML	:	Perfectly Matched Layer
BC	:	Boundary Condition
MUMPS	:	Multifrontal Massively Parallel Sparse Direct Solver
UM	:	University of Malaya
UV	:	Ultraviolet
PID	:	Proportional Integral Deferential
ID/OD	:	Inner wall over outer wall diameter ratio
SEM	:	Scanning Electron Microscope
CCD	:	Charge Coupled Device
RI	:	Refractive Index
FBG	:	Fiber Bragg Grating

LPFG	:	Long Period Fiber Grating
PMF	:	Polarization Maintaining Fiber
OSA	:	Optical Spectrum Analyzer
SPP	:	Surface Plasmon Polaritons

CHAPTER 1: INTRODUCTION

1.1 Overview

Almost four decades have passed since the research on optical fiber sensors started in earnest. Optical fiber sensor technology providing the possibility of sensing various measurands such as temperature, strain, pressure, voltage, current, gas, rotation, chemical contaminant, vibration, acceleration, torsion, bending, displacement and biomolecules (B. Lee, 2003). Detection on the measurand is typically demonstrated by a modulation in phase, power, wavelength or polarization of the received light. Well-known advantages of optical fiber sensors are high sensitivity, compactness, large bandwidth, immunity to electromagnetic interference and light weight. The merits of optical fiber sensors over their electrical equivalents attract research institutions and industries to extensively study and utilize optical sensing in a wide range of applications like medical diagnostics, quality control systems and manufacturing processes.

Optical fiber sensors can be based on fiber gratings, Faraday rotation, interferometers, scattering/reflecting, fluorescence, luminescence, fiber optic gyroscopes, and interaction of evanescent field structures (Mescia & Prudenzano, 2013). The most successful sensors in the early stage of research are the fiber optic hydrophones based on Mach-Zehnder interferometer and fiber optic gyroscopes based on the Sagnac effect (Udd & Spillman Jr, 2011). Gratings are simple and intrinsic sensing elements. They are photo-inscribed into a silica fiber (Hand & Russell, 1990; Hill, Fujii, Johnson, & Kawasaki, 1978; Kashyap, 1994; Meltz, Morey, & Glenn, 1989; Payne, 1989; Stone, 1987). Grating-based sensors have been explored intensively in the area of distributed embedded sensing in materials. This area plays the main role in creating “smart structures”. The health of the structure (measured through parameters such as load, strain, vibration and temperature) can be tracked and assessed on a real-time basis (Kersey et al., 1997). Distributed temperature sensing can be done by Brillouin scattering in silica fibers (Kurashima,

Horiguchi, & Tateda, 1990). Faraday rotation is implemented in magnetic field sensors which have been widely used for vehicle detection, navigation and current sensing (Sun, Jiang, & Marciante, 2010).

Using an optical fiber, the simplest approach for sensing is by transporting light to and from the sensing region. Interaction between light and environment such as absorption and fluorescence occurs to the fiber in such configuration (Monro et al., 2010). Light is primarily confined within the core of a waveguide when the size of the core is greatly larger than the wavelength of the light, with only the tails of the guided mode extending into the surrounding medium. This is usually defined as the evanescent field. Confinement loss is the light confinement ability within the core region. Sensors based on the interaction of this tail of the guided mode with a sensing object are called evanescent field sensors (Ng, Wong, et al., 2017). This thesis focuses on designing and fabricating evanescent field exposed optical fibers which are able to provide high evanescent field exposure with low confinement loss. High evanescent field exposure allows higher interaction while low confinement loss allows longer interaction path and all these lead to a high sensitivity evanescent field sensors.

1.2 Motivation

To date, numerous evanescent field exposed optical fibers have been proposed and studied for sensing purposes. Compared to D-shaped (Stewart, Jin, & Culshaw, 1997) and tapered fiber (Tong et al., 2003), which are environmentally sensitive and fragile, microstructured optical fibers (MOFs) provide longer enclosed interaction path and are more durable due to the fact that the coating of cladding of MOFs do not need to be removed (J. Wang, Jiang, Hu, & Gao, 2007). Various MOF structures have been introduced to provide high evanescent field exposure, for example, defected-core photonic crystal fiber (PCF) (Fini, 2004; Yu et al., 2008; Zhi-guo, Fang-di, Min, & Pei-da, 2008), PCF with hollow high index ring defect at the center (Olyaee, Naraghi, &

Ahmadi, 2014; Park, Lee, Kim, & Oh, 2011), microstructured-core PCF (Cordeiro et al., 2006), and suspended-core holey fiber (Euser et al., 2008; Webb, Poletti, Richardson, & Sahu, 2007). These specially designed MOFs allow high exposure of evanescent field with the trade-off in confinement loss. Other than the issue of confinement loss, the size of air cavities in a MOF is another crucial criterion to be considered since larger size eases the analyte flow and also the coating process which is needed in some sensing applications.

1.3 Objectives

The main objective of this thesis is to design and fabricate evanescent field exposed optical fibers for optical sensing. In particular, the scope of this study is as follows:

1. To design and fabricate a modified PCF which can provide high evanescent field exposure with low confinement loss;
2. To model the modified PCF to determine its performance in terms of evanescent field exposure and confinement loss;
3. To design and fabricate a novel MOF having large cavities while allowing high exposure of evanescent field with low confinement loss; the light guiding ability is to be confirmed via characterization; and,
4. To model the novel MOF as a surface plasmon resonance (SPR) sensor.

1.4 Thesis Outline

This thesis is comprised of seven chapters, including the current introductory chapter. Literature review has been conducted and presented in Chapter 2, introducing the theoretical background of evanescent field sensing and different evanescent field exposed structures proposed by other researchers. Chapter 3 presents the design of the proposed Sunny PCF. It has been modelled to investigate its performance. Chapter 4 describes the stack and draw fabrication method used in fabricating Sunny PCF. A novel MOF, given

the name of Diamond Ring Fiber (DRF) has been introduced in Chapter 5. The design and the fabrication process of DRF have been presented. The same chapter also describes the experimental setup used to characterize DRF and the simulation work done for obtaining its performance. Chapter 6 presents a highly sensitive DRF-based SPR sensor for refractive index sensing. Gold coated DRF is modelled to investigate the wavelength and amplitude interrogation sensitivity over the refractive index range of 1.33-1.39. Finally, Chapter 7 concludes all the important findings in this thesis and explores future works.

CHAPTER 2: LITERATURE REVIEW

2.1 Evanescent Field

The mechanism by which light rays are confined within a waveguide is by total internal reflection and in order to visualize this phenomena closely at the guide cladding interface, it becomes necessary to approach electromagnetic wave theory model at the interface (Syms & Cozens, 1992). The simplest way to understand the concept of optical propagation through the waveguide is by considering the case of planar waveguide structure.

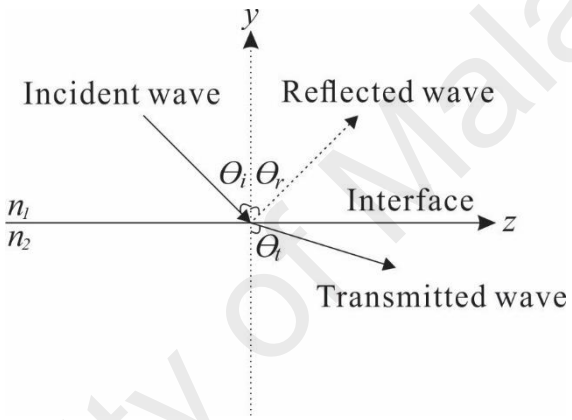

Figure 2.1: Light ray incident on the boundary between two dielectric media with refractive indices n_1 and n_2.

When an electromagnetic wave is incident on the boundary between two dielectric media whose refractive indices are n_1 and n_2, then in general, a portion of that wave is reflected and remainder, transmitted.

$$\nabla^2 \mathrm{E} + n^2 k_0^2 \mathrm{E} = 0 \qquad (2.1)$$

represents the wave equation which is incident from the higher index (n_1) region to the lower index (n_2) region. The wave is incident on the interface at an angle Θ_i to the normal and reflected and transmitted waves are at angles Θ_r and Θ_t respectively. The following equations relate these angles

$$\theta_i = \theta_r \qquad (2.2)$$

$$\frac{\sin\theta_i}{\sin\theta_t} = \frac{n_2}{n_1} \tag{2.3}$$

Across the boundary Maxwell's equation require that both the tangential components of **E** and **H** and the normal components of **D** and **B** are continuous.

$$\mathbf{n} \times (\mathbf{E_2} - \mathbf{E_1}) = 0 \tag{2.4}$$

$$\mathbf{n} \times (\mathbf{H_2} - \mathbf{H_1}) = 0 \tag{2.5}$$

$$\mathbf{n} \cdot (\mathbf{D_2} - \mathbf{D_1}) = 0 \tag{2.6}$$

$$\mathbf{n} \cdot (\mathbf{B_2} - \mathbf{B_1}) = 0 \tag{2.7}$$

where **n** is a unit vector perpendicular to the plane formed by the two vectors. Solving the wave equation with suitable approximations, we will get Fresnel's equations and these equations deal with the magnitudes of the transmitted and reflected electric fields relative to the incident field (Wilson & Hawkes, 1998).

$$\frac{\mathrm{E}_r^{\perp}}{\mathrm{E}_i^{\perp}} = \frac{n_1\cos\theta_i - n_2\cos\theta_t}{n_1\cos\theta_i + n_2\cos\theta_t} \tag{2.8}$$

$$\frac{\mathrm{E}_r^{\parallel}}{\mathrm{E}_i^{\parallel}} = \frac{n_1\cos\theta_t - n_2\cos\theta_i}{n_1\cos\theta_t + n_2\cos\theta_i} \tag{2.9}$$

$$\frac{\mathrm{E}_t^{\parallel}}{\mathrm{E}_i^{\perp}} = \frac{2n_1\cos\theta_i}{n_1\cos\theta_i + n_2\cos\theta_t} \tag{2.10}$$

$$\frac{\mathrm{E}_t^{\parallel}}{\mathrm{E}_i^{\parallel}} = \frac{2n_1\cos\theta_i}{n_1\cos\theta_t + n_2\cos\theta_i} \tag{2.11}$$

where $\mathrm{E}^{\parallel}$ and $\mathrm{E}^{\perp}$ represent electric field vectors parallel and perpendicular to the plane of incidence.

In the situation of total internal reflections, *i.e.*, when $\Theta_i > \Theta_c$ where

$$\theta_c = \sin^{-1}\frac{n_2}{n_1} \tag{2.12}$$

there will not be a transmitted wave in the second medium. Although all the energy in the beam is reflected when $\Theta_i > \Theta_c$, there is still a disturbance in the second medium, whose electric field amplitude decays exponentially with distance away from the boundary. We can derive an expression for this decay by considering the phase factor P of the transmitted wave. P at a point '**r**' may be written as

$$\mathrm{P} = \exp i\,(\omega t - \mathbf{k_t}\cdot\mathbf{r}) \tag{2.13}$$

where, $\mathbf{k_t}$ is the wave vector associated with the transmitted wave.

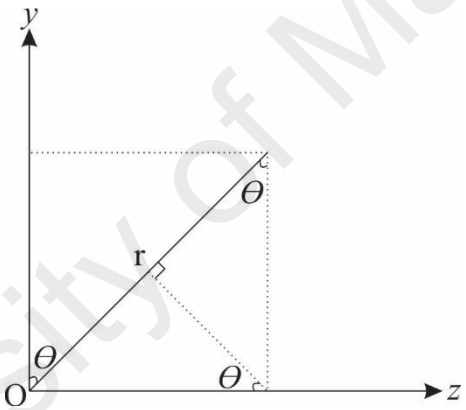

Figure 2.2: Illustration of the relationship between the rectangular coordinates *y* and *z* and the distance r measured from the origin O.

From Figure 2.2, r may be written as

$$\mathrm{r} = z\sin\theta_t + y\cos\theta_t \tag{2.14}$$

Substituting this in Equation 2.13, we get

$$\mathrm{P} = exp\, i\,[\omega t - \mathrm{k_t}(z\sin\theta_t + y\cos\theta_t)] \tag{2.15}$$

$$\mathrm{P} = \exp i\,[\omega t - \frac{2\pi n_2}{\lambda_0}(z\sin\theta_t + y\cos\theta_t)] \tag{2.16}$$

where λ_0 is the wavelength of radiation in vacuum. We have

$$\cos\theta_t = (1 - \sin^2\theta_t)^{1/2} \tag{2.17}$$

From Equation 2.3,

$$\sin^2\theta_t = \frac{{n_1}^2}{{n_2}^2}\sin^2\theta_i \tag{2.18}$$

Hence,

$$\cos\theta_t = [1 - (\frac{n_1}{n_2})^2\sin^2\theta_i]^{1/2} \tag{2.19}$$

when $\Theta_i > \Theta_c$, $\sin\Theta_i > n_1/n_2$ and $\cos\Theta_t$ then becomes wholly imaginary. Then

$$\cos\theta_t = \pm i\mathrm{B} \tag{2.20}$$

where

$$\mathrm{B} = [\left(\frac{n_1}{n_2}\right)^2\sin^2\theta_i - 1]^{1/2} \tag{2.21}$$

Substituting in Equation 2.16 for $\sin\Theta_t$ and $\cos\Theta_t$

$$\mathrm{P} = \exp i\,[\omega t - \frac{2\pi n_2}{\lambda_0}\left(z\frac{n_1}{n_2}\sin\theta_i + (\pm i\mathrm{B})y\right)] \tag{2.22}$$

$$\mathrm{P} = \exp\left(\pm\mathrm{B}\frac{2\pi n_2}{\lambda_0}y\right)\exp i\,(\omega t - \frac{2\pi n_1\sin\theta_i}{\lambda_0}z) \tag{2.23}$$

Thus, in the *y* direction the wave either grows or decays exponentially with distance. The former situation is obviously a nonphysical solution and we must choose

$$\cos\theta_t = -i\mathrm{B} \tag{2.24}$$

The decay with distance in the second medium is given by the factor F(*y*) where

$$\mathrm{F}(y) = \exp(-\frac{2\pi n_2}{\lambda_0}\mathrm{B}y) \tag{2.25}$$

$$\mathrm{F}(y) = \exp(-\frac{2\pi n_2}{\lambda_0}[\left(\frac{n_1}{n_2}\right)^2 \sin^2\theta_i - 1]^{1/2}y) \tag{2.26}$$

Usually F(y) decays rapidly with y. However, when Θ_i is very close to Θ_c, then $[(n_2/n_1)^2 \sin^2 \Theta_i - 1]^{1/2}$ will be close to zero and the disturbance may extend an appreciable distance into the second medium. This part of the wave in the second medium is the evanescent field.

2.2 Evanescent Field Exposed Optical Fibers

2.2.1 Tapered Fiber

Single-mode tapered fibers (SMTFs) have been proposed to develop a variety of sensors (Bariain, Matías, Arregui, & López-Amo, 2000; Bobb, Shankar, & Krumboltz, 1991; Moar et al., 1999; Romolini, Falciai, & Schena, 1998; Shadaram, Espada, Martinez, & Garcia, 1998; Tubb, Payne, Millington, & Lowe, 1995). In a SMTF the gradual reduction of the core and cladding diameters makes the evanescent fields spread out into the cladding and reach the environment. The taper parameters, such as waist diameter, length, and shape, are important when the taper is to be used as a sensor. It is also convenient to control all these parameters during the fabrication process and to know their influence on sensor properties. A fabrication technique that allows precise control of taper parameters has been described (Harun, Lim, Tio, Dimyati, & Ahmad, 2013). This method consists of fusing and stretching an optical fiber with a traveling gas burner. This technique allows the fabrication of tapers with a uniform waist diameter as depicted in Figure 2.3.

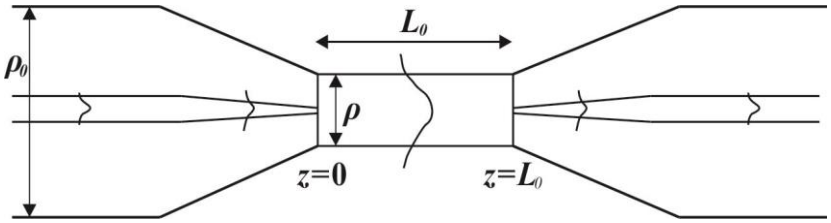

Figure 2.3: Diagram of a tapered optical fiber with a uniform waist. Propagation of the fundamental mode is illustrated.

One can taper an optical fiber of initial diameter ρ_0 to a final diameter ρ by stretching a uniformly heated fiber section of length L_0. The taper waist is predicted to vary with elongation distance z as (Kenny, Birks, & Oakley, 1991)

$$\rho = \rho_0 \exp(-\frac{z}{2L_0}) \qquad (2.27)$$

and the waist is of length L_0. The taper transitions are exponential in shape (Birks & Li, 1992).

2.2.2 D-shaped Fiber

D-shaped optical fibers can be fabricated by removing a portion of cladding (lengthwise) of the optical fiber until the core of the fiber, and hence a strong interaction between the evanescent field of the light signal and the external environment can occur at the polished surface (Lu et al., 2014). Conventionally, a D-sector is produced on optical fibers through polishing techniques. An optical fiber is glued by epoxy in a cut curved V-shaped groove while its cladding is polished away over an interaction length of several millimeters.

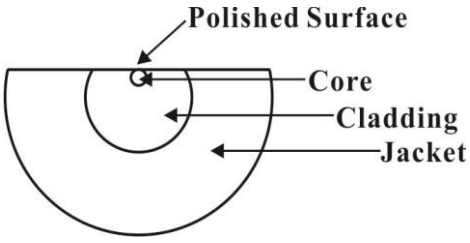

Figure 2.4: Cross-sectional view of a D-shaped fiber.

2.2.3 Microstructured Optical Fiber (MOF)

MOFs are reported in the 1970s as low loss optical fibers for data transmission purposes. They are fabricated from undoped silica glass in such a way that the core is suspended in air by a thin membrane of glass (Kaiser, Marcatili, & Miller, 1973). MOFs consist of a cladding region made up of air holes running along the fiber. This kind of structure allows evanescent wave interaction between the guided mode and any matter inside the air holes. Comparing to aforementioned evanescent field exposed schemes which are environmentally sensitive and fragile, MOFs are more efficient by providing much longer enclosed interaction path and more durable due to the fact that no coating or cladding is needed to be removed (S.-G. Li et al., 2007). MOFs with hollow core are generally referred to as photonic bandgap fibers (PBGFs). PBGFs guide the light in the air core based on photonic bandgap effect. PCFs are MOFs with periodic air holes structure and a defect at the middle. Index guiding PCF has been chosen as a practical sensing tool despite PBGF allows highest interaction strength due to its limited transmission bands and lossy connection with conventional single mode fibers (SMFs) (Hansen et al., 2004). PBGFs require the accurate and stringent control for introducing the band gap effect in its periodic microstructure dimensions (Olyaee & Naraghi, 2013).

2.2.3.1 Photonic Crystal Fiber (PCF)

The missing air hole in PCFs constitutes to an effective index difference between the silica defect and the cladding. This allows PCFs to guide light based on modified total internal reflection, similar to that of conventional SMFs (J. C. Knight, 2003). PCFs are given more interest by researchers compared to SMFs due to their unique optical properties (endlessly single mode, high birefringence, high nonlinearity, engineerable chromatic dispersion and etc.), which can be achieved by carefully choosing PCFs' waveguide parameters: air hole diameter d, pitch size Λ and air filling ratio d/Λ (Russell, 2003).

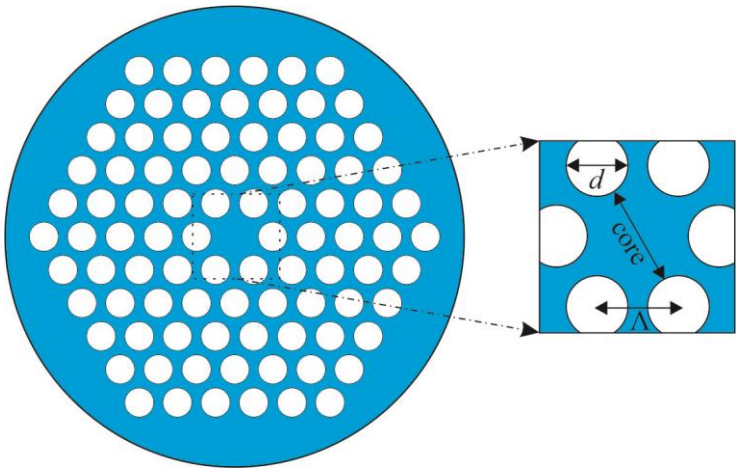

Figure 2.5: A conventional solid core PCF with hexagonal lattice structure. Region in each hole is air whereas region outside the holes is the background silica material.

This thesis is interested in PCF's ability to allow the exposure of evanescent wave to the air holes. Liquid and gas analyte can be infiltrated into PCFs' air holes for the interaction with guided mode. This brings intense research on PCFs as optical sensors (Frazao, Santos, Araújo, & Ferreira, 2008). Sensing capability will be higher when the fraction of power in the air holes is larger. In gas concentration measurement for example, gas species absorbs the evanescent field in the air holes (Hoo et al., 2003) according to

$$f = \frac{\int_{air}(E_x H_y - E_y H_x)\, dx\, dy}{\int_{total}(E_x H_y - E_y H_x)\, dx\, dy} \qquad (2.28)$$

where f is the fraction of the total power located in the air holes (Stewart, Norris, Clark, & Culshaw, 1991), referred to as the evanescent field exposure in this work.

From the work reported in (Monro, Richardson, & Bennett, 1999), evanescent field exposure can be greatly improved without significantly compromising the mechanical structure of PCFs by adjusting Λ and d/Λ in PCFs. Evanescent field exposure of the PCF becomes higher when the Λ is smaller and d/Λ is larger due to the air holes are closer to the core where the guided mode propagates. The effect of changing d/Λ on the evanescent field exposure of the PCFs is only significant when the Λ is relatively small compared to

the wavelength of the guided light (Monro et al., 2001). Conventional solid-core PCF with Λ = 0.75 μm and d/Λ = 0.8 has been simulated at wavelength of 1500 nm and the result showed an evanescent field exposure as high as 30%, but also a high confinement loss of 313.36 dB/m. Confinement loss is the loss arising from the leaky nature of the modes and the non-perfect structure of the PCF fiber. The confinement loss is calculated in terms of the imaginary part of the effective refractive index of the guided mode Im[n_{eff}] and the operating wavelength λ (Saitoh & Koshiba, 2003) as shown below

$$\text{confinement loss} = 8.686 \frac{2\pi}{\lambda} \text{Im}[n_{eff}] \qquad (2.29)$$

2.2.3.2 Defected-Core PCF

Several ideas are reported for improving PCF's sensing performance in terms of the evanescent field exposure and confinement loss. The concept of defected-core PCF as shown in Figure 2.6 has been proposed theoretically for sensing gases and liquids (Fini, 2004). Numerical analysis to relate the sensing performance with the parameter of the defected-core PCF geometry (Zhi-guo et al., 2008) and experimental investigation on it (Yu et al., 2008) has been reported.

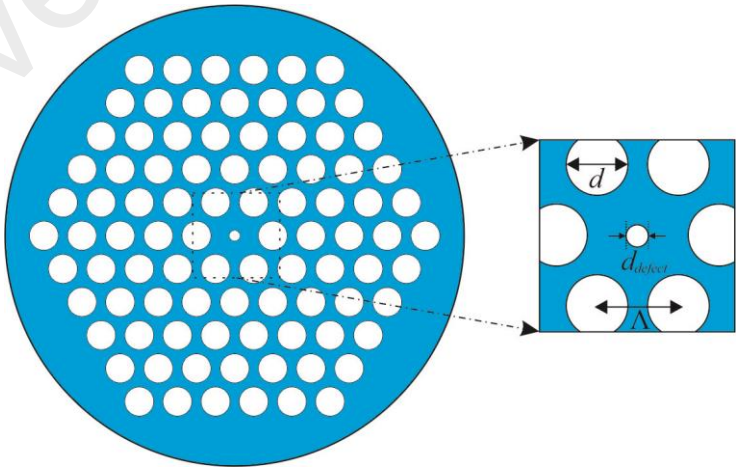

Figure 2.6: Cross-sectional view of a defected-core PCF.

Since the air hole at the middle of the silica core has smaller dimension (d_{defect}) than the dimension of each individual cladding hole, the effective index guiding criterion is still satisfied (Olyaee & Naraghi, 2013). Although the smaller air hole at the middle of the core has enhanced the exposure of evanescent field into the cladding, it introduces large confinement loss at the same time (Zhi-guo et al., 2008). The number of hole layers in the cladding has been then increased to reduce the confinement loss (Ferrarini, Vincetti, Zoboli, Cucinotta, & Selleri, 2002; Saitoh & Koshiba, 2003). Also, enlarging the hole dimension of two outer cladding rings in a 5-ring hole defected-core PCF (Olyaee & Naraghi, 2013) has been demonstrated for the same purpose. A PCF with hollow high index ring defect at the center is introduced (Park et al., 2011) to solve the confinement loss problem in defected-core PCF. With the pitch and air holes of 2.3 μm and 1.4 μm, this fiber has lower confinement loss of 1.25 dB/m at 1500 nm compared to that of prior defected-core PCF (Fini, 2004) with the same structure parameter and the confinement loss of 32.4 dB/m. Hollow high index GeO_2-doped silica ring defect approach has been reported (Olyaee & Naraghi, 2013) to improve the prior PCF (Park et al., 2011). The hexagonal holes instead of circular holes at the center increase the evanescent field exposure from 12.5% to 17.5% at 1500 nm wavelength. However, this is still in a modelling stage since controlling the thickness of the GeO_2-doped silica ring is very challenging during fabrication process.

2.2.3.3 Suspended-Core Holey Fiber

Besides PCFs, some specialty MOFs have also been proposed to be implemented as evanescent field exposed fibers. Core-suspended capillary fiber which the core is suspended in the air space and close to the capillary's inner surface (Zhang et al., 2014) has been reported. Analyte will flow through in the capillary and the evanescent field outside the suspended core will interact with it. Since the core is not located in the middle of the fiber, it requires extra work in the alignment with standard SMFs.

Another specialty all-silica MOF is suspended-core holey fiber (Euser et al., 2008; Monro et al., 2010; Webb et al., 2007) which is having a small core surrounded by three air holes as shown in Figure 2.7 below.

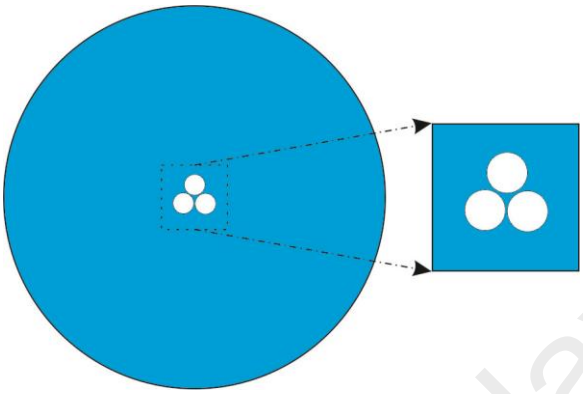

Figure 2.7: Cross-sectional view of a suspended-core holey fiber.

Such suspended-core fiber structure has been demonstrated in bismuth glass using an extrusion technique (Ebendorff-Heidepriem et al., 2004; Kiang et al., 2002). Another method has been proposed to realize this structure in silica (Webb et al., 2007). Ultrasonic drilling is used to define the air holes in a solid silica rod, which is then caned and drawn inside a jacket tube into fiber, using conventional fiber-drawing tower. Suspended-core holey fiber can achieve evanescent field exposure as high as 29% with a core size of 0.8 μm while providing relatively large air holes compared to PCF. It has been known to be the best candidate as an evanescent field exposed structure before our work.

2.2.4 Summary

Each of the reported evanescent field exposed fibers has its own limitations. D-shaped fiber and tapered fiber are environmentally sensitive due to the unprotected interaction path. Besides, their structural design limits the length of the interaction path. Longer interaction path effectively increase the interaction between light and analyte and boost up the sensitivity (Azad, Nikzad, & Parvizi, 2018; Chandra, Dhawangale, & Mukherji, 2018). Tapered fiber is particularly fragile and it is not experiment friendly in terms of

device handling. These are the reasons why MOFs are the preferable structures with their enclosed and long interaction path. However, PCF for example, is having relatively low evanescent field exposure. Intensive research has been done by researchers to modify the PCF structure for increasing the evanescent field exposure. However, it comes with the trade off in confinement loss. Defected-core PCF for instance, the non-gaussian mode field distribution causes the high confinement loss. High confinement loss itself limits the interaction again since light is able to propagates only in limited length before it is totally leaked into the silica cladding. Other than enclosed long interaction path, high evanescent field exposure, and low confinement loss, the cavities size is another crucial feature for an evanescent field exposed fiber. In most of the bio sensing application, SPR phenomenon is playing the important role in detecting the change in refractive index (Rifat, Ahmed, Mahdiraji, Adikan, & Miroshnichenko, 2018). Metal element need to be coated in the fiber for realizing fiber-based SPR sensor, which is less bulky as compared to conventional prism-based SPR sensor. Coating inside the cavities of MOFs will be much easier when the cavities size is relatively larger. Suspended-core holey fiber which is formerly known as the best candidate for evanescent field sensing is lacking of this feature. Before this work, there is no any evanescent field exposed fiber which is able to provide enclosed long interaction path, high evanescent field exposure, low confinement loss, and large cavities in a single structure.

CHAPTER 3: SUNNY PHOTONIC CYRSTAL FIBER

3.1 Design of Sunny PCF

The modified PCFs mentioned in Section 2.2.3.2 require too much change in PCF's conventional hexagonal lattice structure, complicating the practical fabrication process. Some of them even require more than one material in fabrication process other than pure silica. In this work, a sunny structure which can be added into a conventional PCF with a simple additional step in stack-and-draw fabrication technique is proposed to enhance the evanescent field exposure while keeping the confinement loss negligible.

From Figure 2.5, the following equation can be deduced to relate PCF parameters with the core size

$$\Lambda = \frac{\text{core}+d}{2} \tag{3.1}$$

Equation 3.1 can be rearranged and factorized into

$$\text{core} = (2 - \frac{d}{\Lambda})\Lambda \tag{3.2}$$

According to Equation 3.2, the idea suggested by previous study (Monro et al., 2001) to improve the evanescent field exposure of a PCF by reducing the Λ is actually reducing the PCF's core size with a constant d/Λ. Reducing Λ size to achieve smaller core size in a conventional PCF can significantly increase its exposure of evanescent field. However, reducing Λ size will directly introduce a high confinement loss to the PCF as a trade-off. As an alternative way to reduce the core size of a PCF but without causing high confinement loss, we introduced a sunny structure (Ng, Rifat, Wong, Tee, & Mahamd Adikan, 2017) on top of a conventional PCF structure, forming Sunny PCF which has 6 triangular interstitial air holes surrounding the silica core as shown in Figure 3.1.

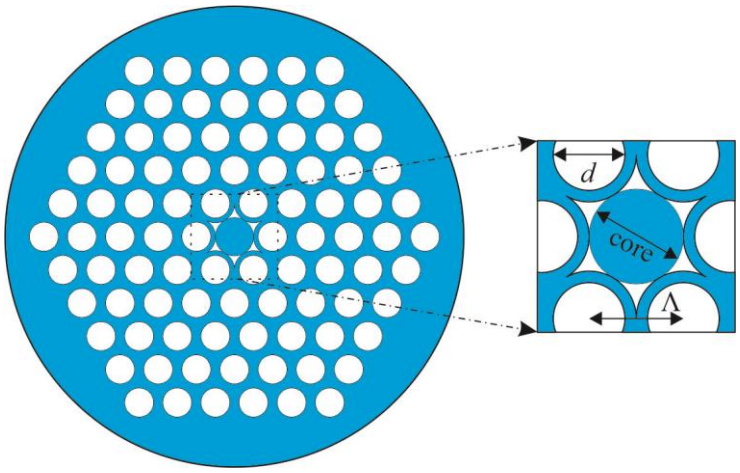

Figure 3.1: Proposed Sunny PCF structure. Magnification shows the triangular interstitial air holes surrounding the silica core to enhance the evanescent field exposure.

This sunny structure can reduce the PCF core size without compromising the original Λ size. Besides solving the problem of high confinement loss due to smaller Λ size, introducing sunny structure (interstitial holes) into the surrounding of the core region can effectively increase the fraction of air region overlapping with the fundamental Gaussian mode profile of the PCF. With more air region overlapping with the guided mode, we can expect higher fraction of light power to be inside the air holes (including interstitial holes). This increment of power fraction is due to part of the guided light will be now directly trapped inside the interstitial holes which enhance the evanescent field exposure without compromising the confinement loss.

3.2 Numerical Simulation

3.2.1 The Maxwell's Eigenvalue Problem

The governing physics of all macroscopic electromagnetism including the propagation of light in PCFs are based on the four Maxwell's equations (Cheng, 1989) as shown below.

$$\nabla \cdot \mathbf{B} = 0 \qquad (3.3a)$$

$$\nabla \cdot \mathbf{D} = \rho \tag{3.3b}$$

$$\nabla \times \mathbf{E} + \frac{\partial \mathbf{B}}{\partial t} = \mathbf{0} \tag{3.3c}$$

$$\nabla \times \mathbf{H} + \frac{\partial \mathbf{D}}{\partial t} = \mathbf{J} \tag{3.3d}$$

where **E** and **H** are the electric and magnetic field intensities respectively whereas **D** and **B** are electric and magnetic flux densities. Assuming the field strength is small so that the analysis is performed in linear regime, the flux densities could be written as

$$\mathrm{D}(r) = \varepsilon_0 \varepsilon(r) \mathrm{E}(r) \tag{3.4a}$$

$$\mathrm{B}(r) = \mu_0 \mu(r) \mathrm{H}(r) \tag{3.4b}$$

where ε_0 and μ_0 are the free space permittivity and permeability respectively, given as ε_0 = 8.854 x 10^{-12} F/m, μ_0 = 4π x 10^{-7} H/m. Speed of light in free space is defined as c = $1/\sqrt{(\varepsilon_0 \mu_0)} \approx 3 \times 10^8$ m/s. $\varepsilon(r)$ and $\mu(r)$ are dimensionless quantities known as relative permittivity and permeability of the medium. Since most dielectric materials of interest have $\mu(r)$ which is very close to unity at optical frequency, for simplicity we define B(r) = μ_0H(r). As a result, ε is the square of the refractive index n. The imaginary part of ε is the material related losses, it is assumed to be zero here considering a low-loss dielectric medium. In the case of no light source, free charges or current in the system, we set ρ = 0 and J = 0. Thus, by taking all these assumptions, Equations 3.3 are rewritten as

$$\nabla \cdot \mathbf{H}(r,t) = 0 \tag{3.5a}$$

$$\nabla \cdot [\varepsilon(r)\mathbf{E}(r,t)] = 0 \tag{3.5b}$$

$$\nabla \times \mathbf{E}(r,t) + \mu_0 \frac{\partial \mathbf{H}(r,t)}{\partial t} = \mathbf{0} \tag{3.5c}$$

$$\nabla \times \mathbf{H}(r,t) - \varepsilon_0 \varepsilon(r) \frac{\partial \mathbf{E}(r,t)}{\partial t} = \mathbf{0} \quad (3.5d)$$

Since Equations 3.5 are linear, the application of Fourier analysis is possible, which means any general solution could be expressed as a set of harmonic modes at different specific optical frequencies. Hence, the temporal dependence could be separated out from the spatial dependence, given as

$$\mathrm{H}(r,t) = \mathrm{Re}[\mathrm{H}(r)e^{jwt}] \quad (3.6a)$$

$$\mathrm{E}(r,t) = \mathrm{Re}[\mathrm{E}(r)e^{jwt}] \quad (3.6b)$$

By substituting Equations 3.6 into Equations 3.5, we obtain two divergence equations and two curl equations, given in Equations 3.7 and 3.8 respectively.

$$\nabla \cdot \mathbf{H}(r) = 0 \quad (3.7a)$$

$$\nabla \cdot [\varepsilon(r)\mathbf{E}(r)] = 0 \quad (3.7b)$$

The two divergence equations indicate no point source nor sink of both electric and magnetic fields in the medium. Also, Equations 3.7 require the field configuration to be transverse, which means the field direction has no component in the propagation direction. The two curl equations relate **E**(*r*) and **H**(*r*).

$$\nabla \times \mathbf{E}(r) - j\omega\mu_0 \mathbf{H}(r) = \mathbf{0} \quad (3.8a)$$

$$\nabla \times \mathbf{H}(r) + j\omega\varepsilon_0 \varepsilon(r)\mathbf{H}(r) = \mathbf{0} \quad (3.8b)$$

By decoupling the Equations 3.8, we obtain an equation only on **H**(*r*), which is known as the master equation, as shown below

$$\nabla \times \left(\frac{1}{\varepsilon(r)} \nabla \times \mathbf{H}(r)\right) = \left(\frac{\omega}{c}\right)^2 \mathbf{H}(r) \quad (3.9)$$

For a given structure with $\varepsilon_r(r)$, the master equation is solved to obtain $\mathbf{H}(r)$ and the corresponding frequencies ω, subject to the transversality requirements in Equations 3.7. Considering longitudinal invariant structures, the solutions are obtain in the form

$$\mathbf{H}(r) = \mathbf{H}(x, y)e^{-j\beta z} \tag{3.10}$$

where β is the propagation constant along the *z*-direction. The eigenvalue problem could be formulated by taking either ω or β as eigenvalue whereas $|\mathbf{H}(x,y)|$ as eigenvector. If the medium is homogenous $\varepsilon(r,\omega) = \varepsilon(\omega)$ with boundary condition between different homogenous regions depends only on single axis in cylindrical or Cartesian coordinates, as in step index fiber, concentric fibers or slab waveguide, Equation 3.9 could be solved analytically as the scalar Helmholtz equation. However, in the case of PCFs, the analytical expression of boundary conditions is too complex. Therefore, numerical methods must be utilized to solve Equation 3.9. For a more comprehensive explanation on Maxwell's eigenvalue problem, please refer to reference (Poletti, 2007).

3.2.2 Numerical Methods

Numerical methods for analyzing waveguides could be divided into two categories, mode solvers and wave propagators. Mode solving methods are based on the assumption that the waveguides are uniform in the propagation direction whereas the wave propagation technique analyses waveguides of changing structures in the propagation direction. Here, mode solving method is considered in analyzing PCFs. A few examples of mode solving techniques are multipole method (MM), plane wave expansion method (PWEM), eigenmode expansion method (EME) and finite element method (FEM).

MM is based on mathematical series of a function that depends on angles, which can be used for full-vector modal calculations of PCFs (Botten et al., 2005). It gives both the real and imaginary parts of the mode propagation constant with the ability to achieve high

accuracy and rapid convergence with modest computational resources. Each dielectric boundary in MM is treated as a source of radiating fields. An advantage of the method is that frequency can be used as input parameter to solve for the propagation constant. This is important in simulation involving dispersive media.

PWEM is a frequency-domain method that formulates eigenvalue problem from Maxwell's equations (Johnson & Joannopoulos, 2001). This method is particularly useful in solving for the band structure of a specific photonic crystal geometry, calculating modal solutions of Maxwell's equations over an inhomogeneous or periodic geometry. The electric or magnetic fields, together with the permittivity are expanded in terms of Fourier series components along the reciprocal lattice vector for each field component. The disadvantage of the PWEM is that the wavevector is used as the input parameter, whereas the frequency eigenvalues are obtained from the calculation. For some applications involving dispersion, it is often more convenient to specify the frequency and solve for the required propagation constant.

EME is a linear frequency domain method that relies on the decomposition of the electromagnetic fields into a set of local eigenmodes that exists in the cross section of waveguide (Gallagher & Felici, 2003). The algorithm is inherently bi-directional and utilizes the scattering matrix technique to join different section of the waveguide. Therefore, all reflections are taken into account. The method can simulate light propagation at any angle even 90 °. Yet, EME is limited to linear problems, nonlinear problems may be modelled using iterative techniques.

FEM is a numerical technique for finding the approximate solutions of partial differential equation (PDE) to handle complex boundary value problems (Koshiba, 1992). The field region is divided into elemental shapes, such as triangles and rectangles, named as finite elements to approximate a more complex equation over a larger domain.

The solution approach is based either on eliminating the differential equation completely as in steady state problems or rendering the PDE into an equivalent ordinary differential equations. A commercial FEM software, COMSOL Multiphysics, is used in this work.

3.2.3 Modelling

The modelling is conducted at the wavelength λ ranged from 800 nm to 2000 nm. Sunny PCF and conventional PCF with different d/Λ are to be modelled to investigate the effect of changing Λ towards evanescent field exposure and confinement loss. Figure 3.2 shows the flow diagram of the processes in simulation.

Figure 3.2: Flow diagram of the various steps in simulation.

3.2.3.1 Geometrical Definition

Full structure has been considered in this work in order to investigate the existence of higher order mode. The required shapes (hexagons, circles, etc.) are drawn through the settings of the dimensions (height and width) and the positions (x, y). Here, circle with the same diameter d are drawn and positioned on the desired lattice with constant pitch Λ as shown in Figure 3.3.

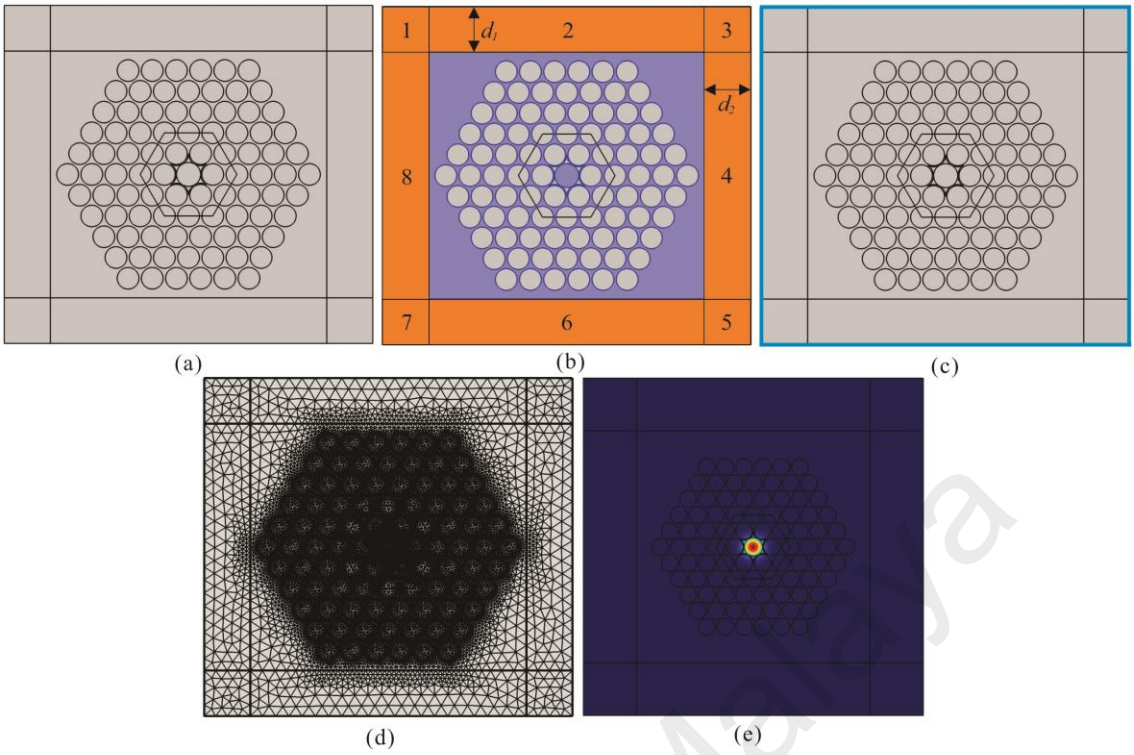

Figure 3.3: FEM simulation on Sunny PCF: (a) structural design; (b) subdomain definition; (c) setting of the boundary conditions; (d) mesh generation; (e) solution.

The boundaries of Perfectly Matched Layers (PML), used to avoid reflections from the outer boundaries and emulate an infinite structure with a finite domain, also need to be drawn at this stage. Depending on the formulation, either square as shown in Figure 3.3(a) or circular shapes can be employed.

3.2.3.2 Subdomain Setting

The physical properties of the material in each subdomain need to be set. The grey holes in Figure 3.3(b) indicate the air region (refractive index equal to 1), while the purple region corresponds to glass, whose refractive index can be set as function of frequency using the Sellmeier equation (Agrawal, 2007)

$$n^2(\omega) = 1 + \sum_{j=1}^{m} \frac{B_j \omega_j^2}{\omega_j^2 - \omega^2} \qquad (3.11)$$

where the m resonant frequencies ω_j and the strength of their resonances B_j depend on the glass.

The external, orange layers are the PMLs introduced to limit the computational domain. PMLs are absorbing layers, specially designed to introduce no reflections for any angle of incidence, polarization or frequency of the incoming electromagnetic radiation, and are therefore perfectly suited to surround the simulation area. Their original concept is introduced by Berenger in 1994 (Berenger, 1994), even though in that first definition they required the local modification of Maxwell's equations. Shortly after, Sacks *et al.* demonstrated that the same absorbing and reflectionless behavior could be achieved without modifying Maxwell's equations, provided that the material is appropriately defined as anisotropic and complex (Sacks, Kingsland, Lee, & Lee, 1995). This approach is much more easily implemented into standard numerical methods and immediately gained much popularity.

According to Sacks, the PMLs are defined as anisotropic materials, whose permittivity and permeability diagonal tensors are (Sacks et al., 1995)

$$[\varepsilon] = \varepsilon_0 n^2 [\Lambda] \tag{3.12a}$$

$$[\mu] = \mu_0 [\Lambda] \tag{3.12b}$$

with

$$\Lambda = \begin{bmatrix} \frac{s_y}{s_x} & 0 & 0 \\ 0 & \frac{s_x}{s_y} & 0 \\ 0 & 0 & s_x s_y \end{bmatrix} \tag{3.13}$$

where ε_0 and μ_0 are the permittivity and permeability of free space, n is the refractive index of the adjacent region and the PML parameters s_x and s_y are defined (Saitoh & Koshiba, 2001) in Table 3.1 for region 1, 2, 3, 4, 5, 6, 7, and 8 in Figure 3.3b.

Table 3.1: PML parameters.

PML parameter	PML region							
	1	2	3	4	5	6	7	8
s_x	s_1	1	s_2	s_2	s_2	1	s_1	s_1
s_y	s_3	s_3	s_3	1	s_4	s_4	s_4	1

Here s_i (i = 1, 2, 3, 4) must be a complex number, the real part of which attenuates potential evanescent waves, while the imaginary part is effective in damping the propagating waves. In many studies (including the present one) the imaginary part is modelled by a polynomially increasing profile, so that

$$s_i = b + ja_{max}\left(\frac{\rho}{d_i}\right)^{\alpha} \tag{3.14}$$

where ρ is the distance from the beginning of the PML, d_i (i = 1, 2) is the PML width in the horizontal or vertical direction, b, a_{max} and α are PML free-parameters. After a number of tests and according to a frequent convention in preceding studies it is decided to fix a parabolic profile (α = 2) with b = 1 for all simulations. A number or convergence test on the best value of a_{max} are also conducted; these are reported in Section 3.2.4.

3.2.3.3 Boundary Setting

The physical properties of all boundaries of the simulation domain then have to be set. The boundary condition (BC) at an edge outside the PML (in blue in Figure 3.3(c)) is generally irrelevant, as the field at that point has been attenuated to a negligible level. Therefore the BCs for a full-structure simulation can be set arbitrarily.

Internal boundaries between subdomains (in black in Figure 3.3(c)) need, in COMSOL Multiphysics, to be assigned the 'internal boundary' condition, which guarantees the continuity of both Displacement and Magnetic fields at the interfaces.

3.2.3.4 Meshing

Several mesh parameters can be adjusted, ultimately determining both accuracy of the solution and calculation time. As a general rule, a large number of triangles need to be positioned both around curved boundaries, in order to accurately define their shape, and where high accuracy is needed (e.g. where the field is more concentrated or where it changes more rapidly). An example is provided in Figure 3.3(d) where an inner hexagonal zone has been defined around the core with the only purpose of allowing a denser mesh. Generally a mesh convergence test is required in order to ensure that the structure has been properly meshed, and to minimize the related numerical errors (see Section 3.2.4).

3.2.3.5 Solving

The COMSOL Multiphysics utilizes MUMPS (MUltifrontal Massively Parallel sparse direct Solver) as a direct solver for eigenvalue problems. Once the solver is chosen, the most important parameters to be defined are the guess for the eigenvalue and the number of eigenvalues to be calculated around this value. For example, in the modal analysis of Sunny PCF, the estimated effective index n_{eff} is the guess for the eigenvalue.

3.2.4 Accuracy

In order to validate the method, convergence tests are run for the main free-parameters of the algorithm: the size of the finite element mesh and the PML parameters. As is mentioned in the previous Section, it is generally a widespread practice to fix $\alpha = 2$ and $b = 1$ in the PMLs (see for example (Saitoh & Koshiba, 2001)). Therefore the parameters whose convergence will be analyzed in the following are the maximum value of the imaginary part of s_i, a_{max}, and the size of the finite element mesh.

The general practice to validate a numerical method would be to test its results against a known analytical result. However as has been previously observed, no analytical results are available for MOFs; furthermore comparisons with the analytical solution of, for

example, a step index fiber would be inadequate for testing the imaginary part of the propagation constant. It has become a common practice therefore, to validate a numerical code by comparison with the results obtained with the method which is recognized as the most accurate MOF modelling: the multipole method. The most employed 'benchmark' for such comparisons is typically the fiber with a single ring of 6 equally spaced holes studied at λ = 1450 nm (White et al., 2002) and presenting Λ = 6.75 µm and d = 5 µm. The silica refractive index is assumed to be n = 1.45.

Figure 3.4 compares the effective index calculated by the MM (n_{eff} = 1.445395345 + j3.150 x 10^{-8}) with the results obtained with the FEM for increasing values of a_{max}. A full structure with a mesh of 173312 triangles, denser in the core, have been used for the FEM.

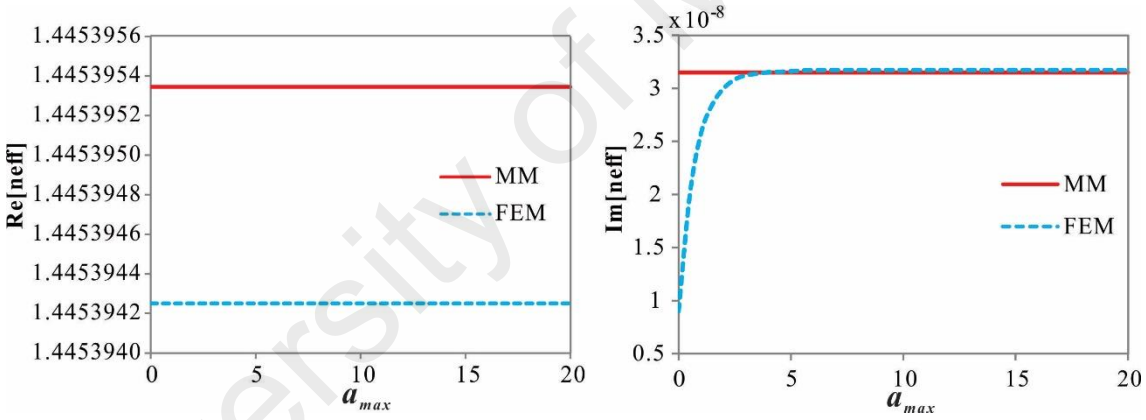

Figure 3.4: Effective index dependence on a_{max} for the fundamental mode of the fiber studied in (White et al., 2002), calculated with the FEM (blue); the MM result is shown in red for comparison.

The real part of n_{eff} is almost unaffected by the change of a_{max}, while a good convergence of Im[n_{eff}] is observed for a_{max} larger than 5. A value of a_{max} = 10 will be therefore employed for all future simulations.

The n_{eff} convergence as a function of mesh density is shown in Figure 3.5 for the same fiber and with a_{max} = 10.

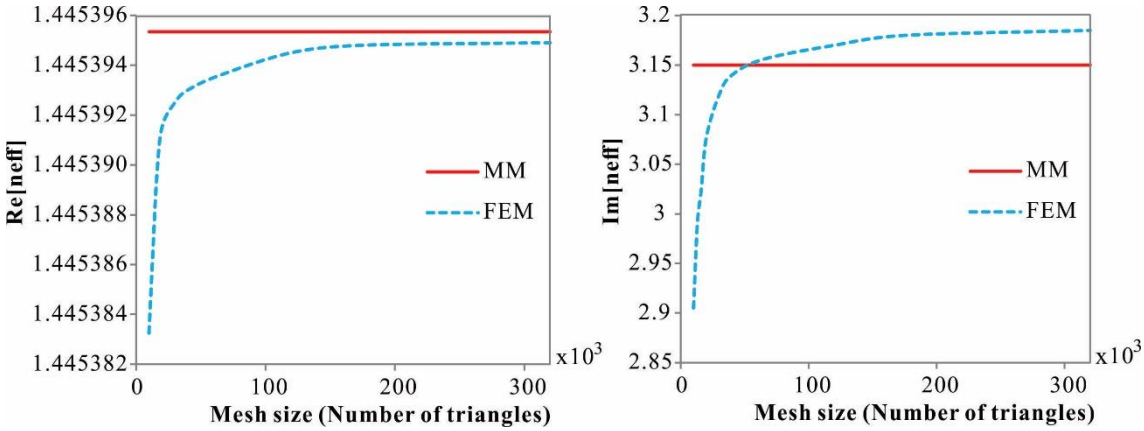

Figure 3.5: Effective index dependence on the mesh size for the fundamental mode of the fiber studied in (White et al., 2002), calculated with FEM (blue); the MM result is shown in red for comparison.

Both Re[n_{eff}] and Im[n_{eff}] are affected by an increase in the number of points, but for a number of triangles greater than ~160000 they both seen to have converged to a stable value. For this converged value the difference in the real part of n_{eff} between two methods lies in the 6th significant digit (~1 x 10^{-6}), while the error in the imaginary part is around 1 x 10^{-10}, corresponding to a variation of less than 1% in the calculated confinement loss.

The level of accuracy found for our implementation of the FEM is therefore in line with that of other numerical methods. For all the studies reported in this thesis it is well above the accuracy that can be obtained in practice when modelling fabricated fibers.

3.3 Results and Discussion

With the same design parameters (Λ, d and d/Λ), Sunny PCF is having a smaller core compared to a conventional PCF. With the additional interstitial holes surrounding the core in Sunny PCF, evanescent field penetrates into the air forming 'side' lobes instead of decaying into the silica between air holes as shown in Figure 3.6. Hence, Sunny PCF is able to achieve higher evanescent field exposure than a conventional PCF over a wide range of wavelength as shown in Figure 3.7. According to Figure 3.7, evanescent field exposure of Sunny and conventional PCFs are 6.52% and 3.31%, respectively while the wavelength is 1550 nm.

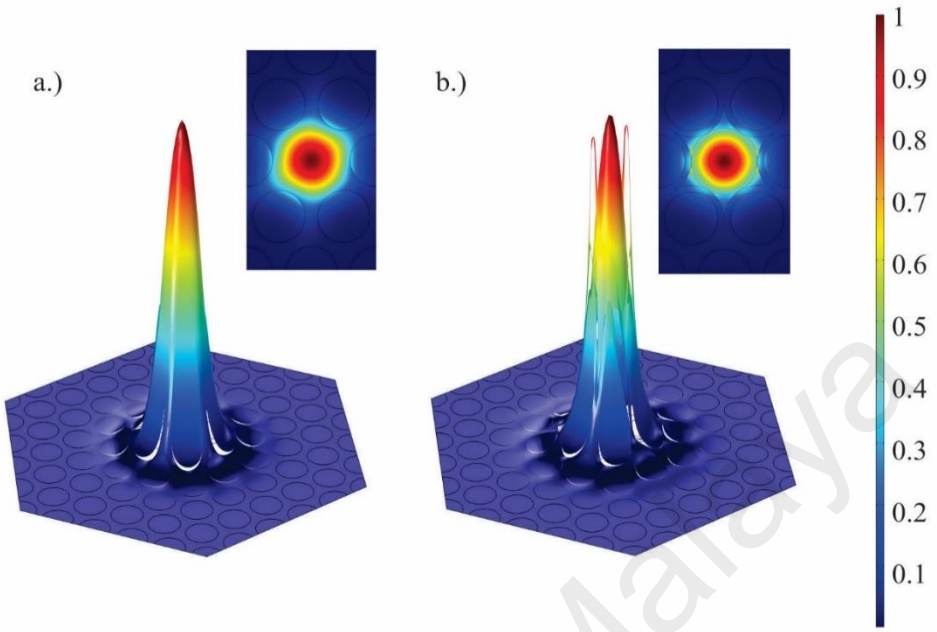

Figure 3.6: Electric field profile of the fundamental mode in (a) conventional PCF and (b) Sunny PCF with Λ = 1.75 µm and *d*/Λ = 0.8 at λ = 1550 nm.

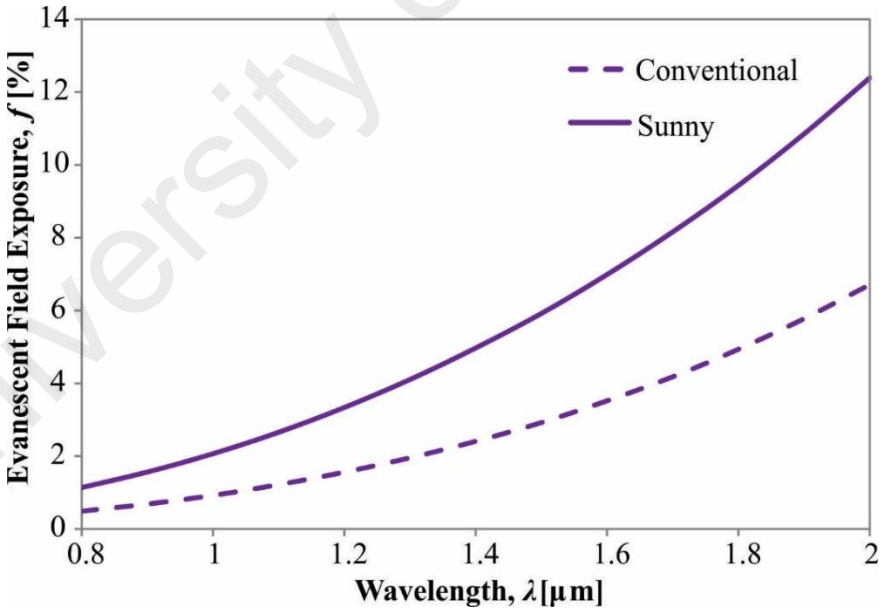

Figure 3.7: Evanescent field exposure, *f* of conventional PCF and Sunny PCF with Λ = 1.75 µm and *d*/Λ = 0.8.

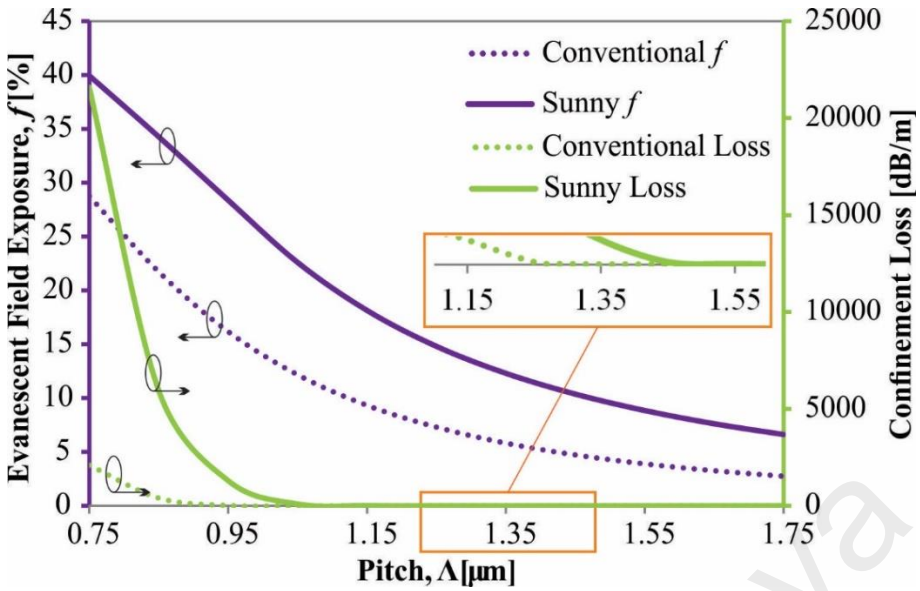

Figure 3.8: Evanescent field exposure, *f* and confinement loss of conventional PCF and Sunny PCF with *d*/Λ = 0.7 at 1550 nm.

Figure 3.8 shows the evanescent field exposure and confinement loss of a conventional PCF and a Sunny PCF with $d/\Lambda = 0.7$ at $\lambda = 1550$ nm. With a very small Λ, both the conventional PCF and Sunny PCF experience an extremely high confinement loss, especially the Sunny PCF which is having a smaller core with the same Λ. This is because when the core is too small compared to the λ, the confinement loss will be extremely high since the light is no longer guided. Although Sunny PCF requires a larger Λ for the confinement loss to be negligible, the Sunny PCF can generally provide a higher evanescent field exposure compared to that of the conventional PCF over the Λ considered. For $\Lambda \geq 1.45$ μm, the evanescent field exposure of a PCF can be improved by adding the sunny structure with negligible confinement loss. The highest achievable evanescent field exposure with negligible loss of a PCF with $d/\Lambda = 0.7$ can be boosted from 7.31% to 10.37% by introducing the first ring interstitial triangular holes in a conventional PCF as shown in Table 3.2.

Table 3.2: Performance comparisons of conventional PCF and Sunny PCF with different *d*/Λ at 1550 nm.

d/Λ	PCF	Pitch, Λ[μm]	Air hole diameter, *d*[μm]	Evanescent field exposure, *f* [%]	Confinement loss [dB/m]
0.7	Conventional	1.25	0.875	7.31	<0.01
	Sunny	1.45	1.015	10.37	<0.01
0.8	Conventional	1.15	0.920	10.48	<0.01
	Sunny	1.25	1.000	13.72	<0.01
0.9	Conventional	1.05	0.945	15.83	<0.01
	Sunny	1.05	0.945	21.23	<0.01

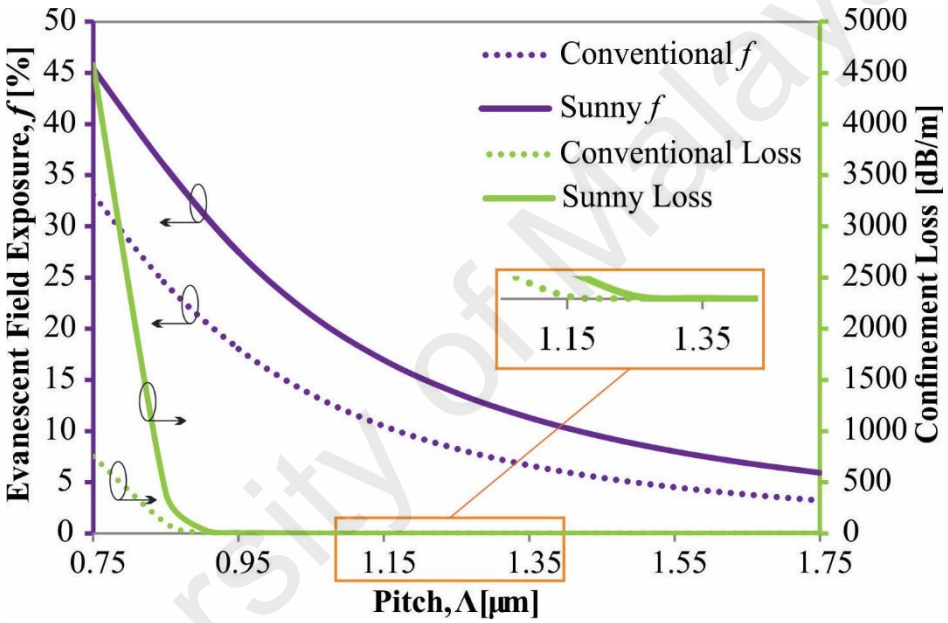

Figure 3.9: Evanescent field exposure, *f* and confinement loss of conventional PCF and Sunny PCF with *d*/Λ = 0.8 at 1550 nm.

Figure 3.9 shows the evanescent field exposure and confinement loss of conventional PCF and Sunny PCF with *d*/Λ = 0.8 at 1550 nm. As the *d*/Λ is increased from 0.7 to 0.8, the light confinement becomes stronger. PCF with larger *d*/Λ indicates higher effective refractive index difference between the core and the cladding. The confinement loss in both the conventional PCF and Sunny PCF tends to be negligible at smaller Λ. This effect is more significant in Sunny PCF with the aid of sunny structure. Larger *d*/Λ also improves the evanescent field exposure for both conventional PCF and Sunny PCF. In conventional PCF, larger *d*/Λ at a particular Λ can provide larger *d* and a smaller core

(less significant compared to adjusting Λ according to Equation 3.2) which allow more evanescent field to be penetrated into air region. In Sunny PCF, larger d/Λ at a particular Λ can provide larger d and more evanescent field can reach the interstitial air holes in the sunny structure. For $\Lambda \geq 1.25$ μm, the evanescent field exposure of a PCF can be improved by adding the sunny structure with negligible confinement loss. The highest achievable evanescent field exposure with negligible loss of a PCF with $d/\Lambda = 0.8$ can be boosted from 10.48% to 13.72% by introducing the first-ring interstitial holes (sunny structure) in a conventional PCF as shown in Table 3.2.

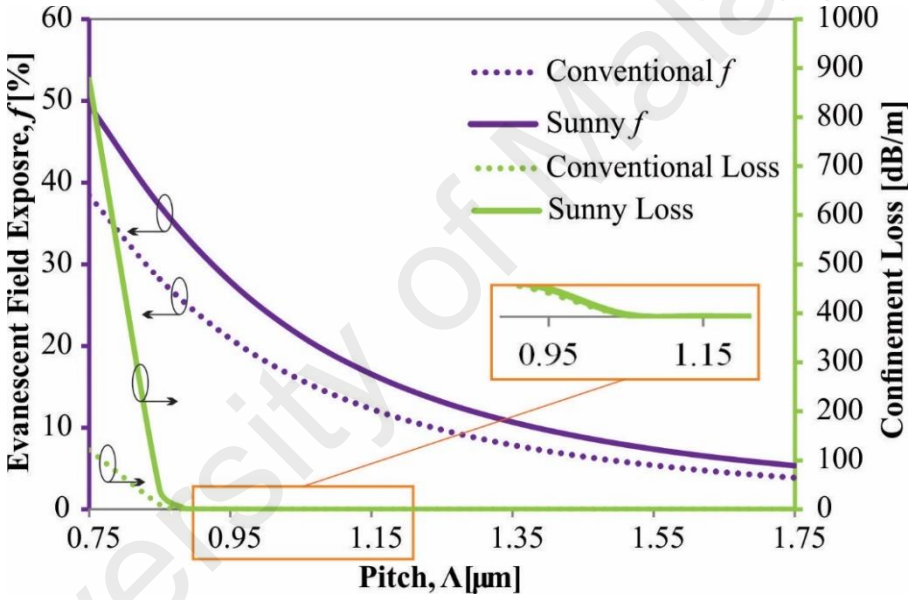

Figure 3.10: Evanescent field exposure, *f* and confinement loss of conventional PCF and Sunny PCF with $d/\Lambda = 0.9$ at 1550 nm.

Figure 3.10 shows the evanescent field exposure and confinement loss of conventional PCF and Sunny PCF with $d/\Lambda = 0.9$ at 1550 nm. With $d/\Lambda = 0.9$, both the conventional PCF and Sunny PCF achieve negligible loss at the same $\Lambda = 1.05$ μm as indicated in the zoom-out box in Figure 3.10. The evanescent field exposure for both conventional PCF and Sunny PCF are further improved with $d/\Lambda = 0.9$. For $\Lambda \geq 1.05$ um, the evanescent field exposure of a PCF can be improved with negligible confinement loss by adding the sunny structure. The highest achievable evanescent field exposure with negligible loss of

a PCF with $d/\Lambda = 0.9$ can be boosted from 15.83% to 21.23% by introducing the first ring interstitial holes in a conventional PCF as shown in Table 3.2.

With larger d/Λ, higher evanescent field exposure can be achieved with negligible confinement loss. Fabrication of PCF with capillaries' d/Λ larger than 0.9 is very challenging since the furnace pressure will easily cause the distortion in air holes structure. So, from all the simulation results above, Sunny PCF with $d/\Lambda = 0.9$ and $\Lambda = 1.05$ is the best design to be implemented in any sensing which requires high light-matter interaction with negligible confinement loss.

In previous works (Euser et al., 2008; Webb et al., 2007), suspended-core holey fiber has been shown to be the best candidate for evanescent field enhancement. Suspended-core holey fiber can achieve evanescent field exposure as high as 29% with core diameter = 0.8 μm at wavelength of 1550 nm (Webb et al., 2007). As shown in Figure 3.10, Sunny PCF can achieve the same evanescent field exposure with a larger core diameter = 0.95 μm ($\Lambda = 0.95$ μm). Larger core size helps to ease the coupling process during experiment and reduce the coupling loss. Furthermore, suspended-core holey fiber reported in (Webb et al., 2007) can achieve evanescent field exposure of 11.5% with core diameter = 1.2 μm at 1550 nm with a confinement loss of 0.29 dB/m. The high loss is due to surface roughness from the ultrasonic drilling during the fabrication process of suspended-core holey fiber (Webb et al., 2007). This issue can be greatly reduced by using stack-and-draw fiber fabrication technique (Ma, Hanzawa, Tsujikawa, Aozasa, & Yamamoto, 2015) which has been implemented in the fabrication of suspended-core holey fiber (Euser et al., 2008). In next chapter, the stack-and-draw technique used in our work will be described. From our simulation, Sunny PCF can achieve the same evanescent field exposure but with a larger core diameter = 1.33 μm and negligible confinement loss as shown in Figure 3.10. Hence, Sunny PCF can achieve the same evanescent field exposure

as suspended-core holey fiber does with a larger core for lower coupling loss and lower confinement loss.

3.4 Fabrication Methods

PCFs have been successfully produced by a number of distinct methods. Generally, they involve preparing a macroscopic meter-length preform with the desired transverse crystal lattice pattern, followed by pulling the preform in high temperature radiation heating furnace to produce microscopic-scale fibers while preserving the intended cross-sectional design. Examples of typical PCF fabrication methods include stack-and-draw (J. Knight, Birks, Russell, & Atkin, 1996), extrusion (Kumar et al., 2002), sol-gel casting (El Hamzaoui et al., 2011) and slurry casting (Yajima et al., 2013). The most common method is stack-and-draw. The process is relatively fast, clean, low-cost, and flexible. It is suitable for creating PCF prototypes, enabling rapid exploration of new PCF structures as well as incorporating different materials into PCF. In this chapter, fabrication of Sunny PCF using stack-and-draw technique is described in detail.

Stack-and-draw process begins with fabricating capillaries of required sizes with specific inner wall over outer wall diameter ratio (ID/OD) based on Sunny PCF d/Λ determined in design. The fabricated capillaries are arranged into triangular lattice using custom-made jigs. By using fiber draw tower, the assembled Sunny PCF preform is pulled into standard fiber format by adjusting carefully the feeding rate, tractor speed, vacuum pressure and furnace temperature.

3.5 Fiber Draw Tower

A 5 m height fiber draw tower in Faculty of Engineering, University of Malaya (UM) with furnace radiation heating capability up to 2700 ℃ is used in this work. The fiber fabrication facility also includes a high-precision motorized chuck, vacuum/pressure system, pyrometer, cane pullers, coating unit, fusion ultraviolet (UV) curing system, laser

diameter gauge, capstan wheels with built-in tension monitor, dancers, drum winder and furnace chiller. The schematic and pictures of the fiber draw tower are shown in Figure 3.11 and Figure 3.12. The fabrication procedures of standard optical fibers are outlined as follows.

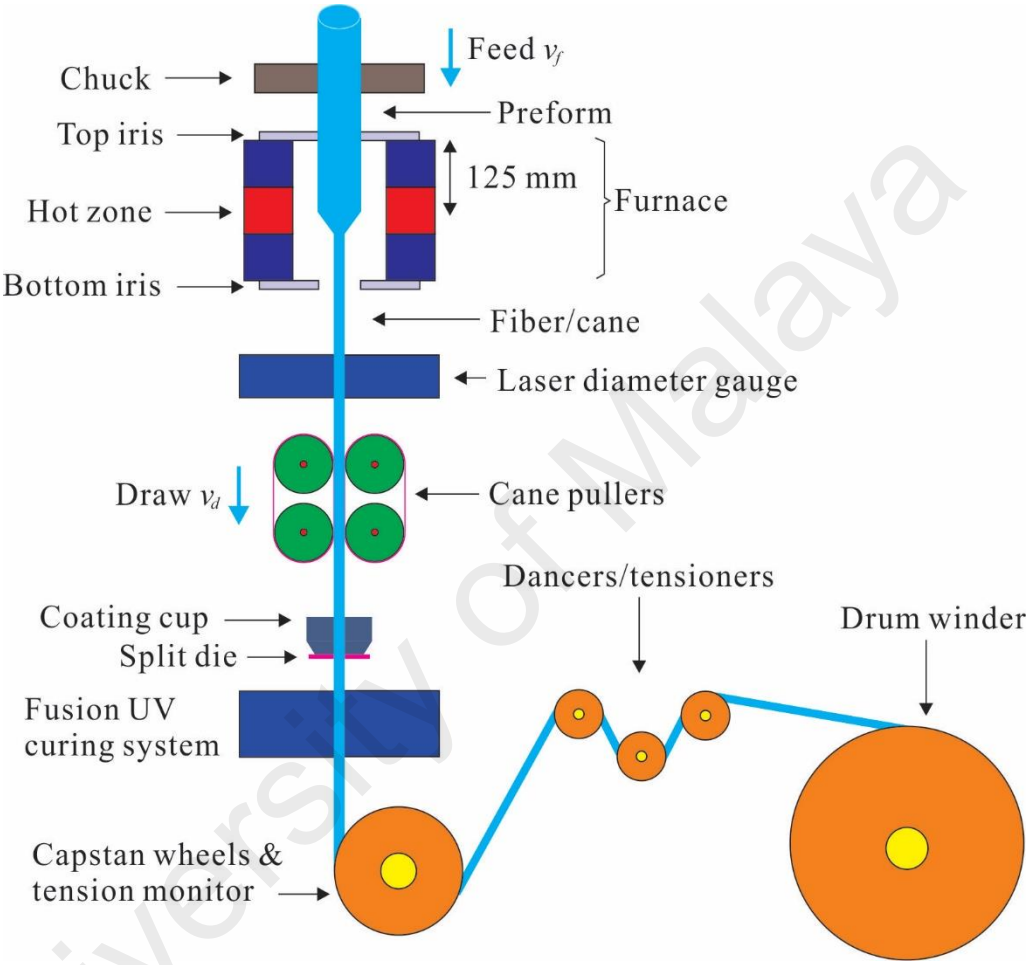

Figure 3.11: Schematic of fiber draw tower in UM.

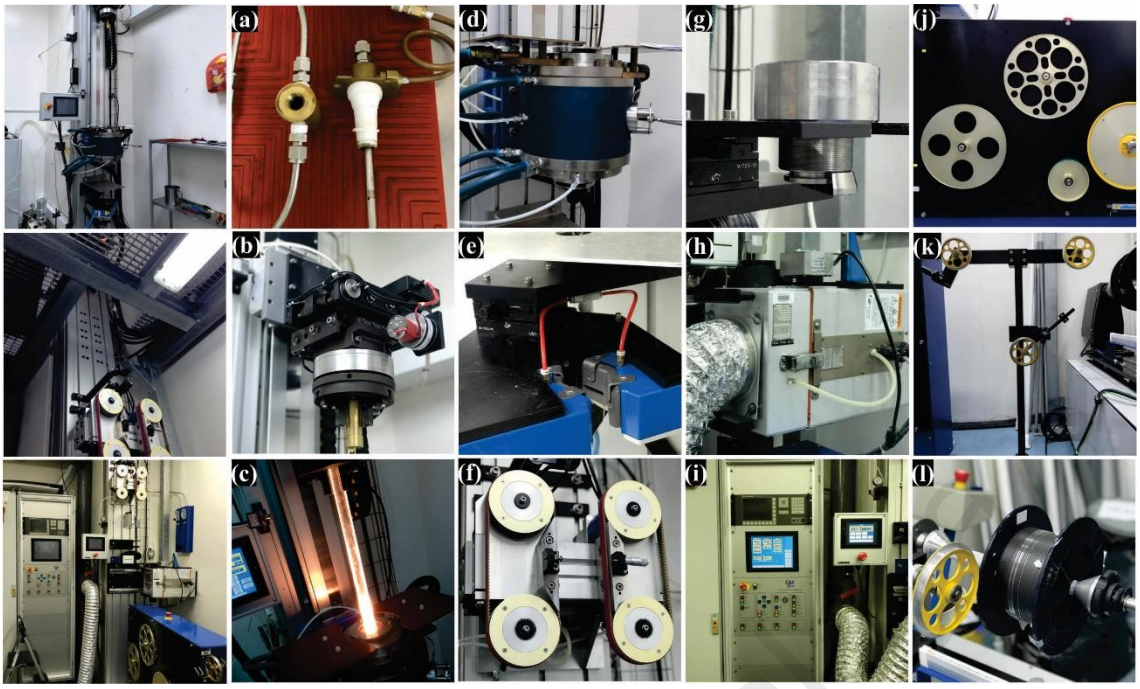

Figure 3.12: The parts of fiber draw tower. (a) Vacuum/pressurization mount, (b) motorized chuck, (c) PCF preform, (d) furnace, (e) laser diameter gauge, (f) tractor/cane pullers, (g) coating cup & split dies, (h) fusion UV curing system, (i) main control cabinet, (j) tension monitor & capstan wheels, (k) dancers/tensioners and (l) drum winder.

Before fiber drawing, the furnace is vacuumed and purged by argon gas to eliminate impurities and prevent oxidization of the heating elements. Argon gas is set to flow continuously after purging to create a low oxygen environment in the furnace. Subsequently, fiber preform is fixed firmly at the high precision motorized chuck, which has the capability of feeding preform at 0.2-20 mm/min with 0.1 mm/min resolution. The furnace's top iris is opened and the fiber preform is lowered slowly until it reaches the same level as the furnace's top opening. Transverse *x-y* position of the preform is adjusted to the center of the furnace bore. Then, vertical position of the preform is reset and the preform is loaded into the furnace for a length of about 160 mm. Vertical position of the heat zone from the furnace top entry is 125 mm. Therefore, the preform drop will be about 35 mm in length. When the preform is in position, furnace temperature is set to ramp up gradually from room temperature to the silica melting point, 2100 ℃. About 10 minutes is required for the furnace to reach the melting point. The furnace temperature is read by

a pyrometer installed at the furnace's heat zone, which has temperature range of 350-2500 ℃ with 1 ℃ resolution.

At melting point, the section of fiber preform at the heat zone develops neck-down profile and starts to drop. The preform drop generates gravitational force that elongates the fiber preform, resulting in a long section which is greatly reduced in diameter. Depending on the mass per unit length of preform, the time taken for the preform drop to exit the furnace's bottom opening may vary from 10 to 15 minutes. Assuming the same lengths of preform drops, those with larger mass per unit length will require more time for heat absorption before melting. Yet, the extended time is compensated by the large mass per unit length of the drop from the same preform which induces greater gravitational force and in turn precipitate the drop process. As the preform drop starts to fall, the round heat illumination through the small opening of bottom iris will expand in diameter. Noticing this indication, the bottom iris must be opened immediately to let the preform drop pass through. The preform drop is then collected in a metal container and cut at the neck-down section as shown in Figure 3.13.

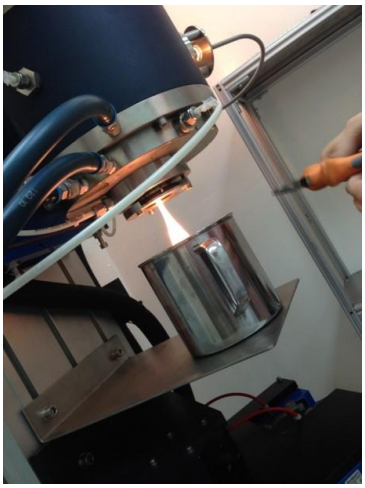

Figure 3.13: Neck-down section of the prefrom.

The cut section is pulled gently by hand to reach the cane pullers. Alternatively, a small weight could be attached to the end of the cut section to give a constant and slow pulling

speed. The cane pullers are set to clamp as the cut section reaches their central position. Subsequently, micro-screw controlling the spacing between the cane pullers are adjusted carefully to give a gentle grip to the cane, followed by starting the feeding and drawing speed simultaneously. If the preform is a cane, feeding speed should begin immediately after cutting preform drop to prevent breaking of fiber inside the furnace, which lead to unnecessary wastage of another preform drop. Feed rate and draw speed are set according to the simplified mass conservation equation to obtain approximate final sizes. The size of fiber/cane is measured in-line by a laser diameter gauge (Zumbach USYS 2100, ODAC 18XY), which can read diameter in the range of 0.08-18.00 mm with resolution of 0.1 μm.

For optical fiber pulling, the fiber size is first adjusted to reach around the intended size by using the cane pullers, followed by winding the fiber according to the predefined route starting from the tension meter, then to the capstan wheels, dancers and finally to the drum winder. After winding is completed, cane pullers are unclamped and capstan wheel is set to turn at the specified draw speed. As the size of fiber stabilizes at the intended diameter, acrylate coating could be applied to the fiber. A coating cup with split die of 375 μm diameter orifice is used, together with the fusion UV curing system. The UV lamp power is controlled automatically with respect to the draw speed.

Further details on optical fiber fabrication are outlined in (Izawa & Sudo, 1987; T. Li, 2012). Here, some additional practical aspects pertaining to fiber fabrication in UM are discussed. The fiber drawing facilities are installed in a cleanroom environment. Humidity and room temperature are set as 50 Rh% and 24 ℃ respectively. In the event where preform vacuum or pressurization is needed, a custom-made preform mount is used to facilitate air tight gas transport between the vacuum/pressurization outlet pipes and preform tube. The preform mount was made from brass and was designed to fit the

preform size, the inner structure consists of a hollow shaft with top and side openings. The weight of preform mount alone could ensures air-tight contact with the preform tube. No rubber contact is used in preform mount as the thermoplastic behavior of rubber prevents it to withstand high temperature.

Throughout the whole process, both the top and bottom irises should be closed to avoid oxidation of the furnace's element. Due to the absence of automatic temperature ramping feature between two intermediate temperatures, manual change of temperature of more than 200 ℃ should be made in a gradual manner (less than 50 ℃ per step) as any sudden and large shift of temperature may shorten the lifetime of the heating element. In order to avoid breaking of fiber in the beginning of pulling, the draw speed should start from 1 m/min and increase slowly towards the intended speed. The laser diameter gauge is set to display the fiber's *x* and *y* axis diameter and its ovality. In fabricating PCFs, ovality is a key indicator of the structural deformation.

In the event of drawing preforms with small diameter less than 5 mm, the preform should be extended out of the bottom iris as the small preform weight will result in long waiting time for drop. In this case, when temperature reaches the melting point, the drop should be pulled down manually by hand. Using a dicing pen or ceramic cutter, short fiber samples are cut for every few meters of fiber length and viewed under the microscope to ensure their quality. The fiber is then inserted through the coating cup and fusion UV curing system. However, coating process does not start at this step.

When the fiber size stabilizes, the drawing force is changed from cane pullers to capstan wheels. This process requires the presence of two operators, one person manually directs the fiber leading end to capstan wheels while another person unclamps the cane pullers and starts the capstan wheels simultaneously from the main control cabinet. Subsequently, the two split dies are attached to the coating cup slowly, the grove on split

dies are aligned carefully to the moving fiber and tightened gently. Automatic transverse *x-y* alignment is activated to ensure fiber passes through the exact center position of the coating cup, preventing fiber fracture due to scratching with split dies. The coating material used in this work is acrylate, the solution is heated up in a water bath at 50 ℃ for eight hours before coating. Depending on the amount needed, some solution is poured into the coating cup and the fusion UV curing system is set to operate immediately.

Fiber tension is monitored continuously throughout the whole process. When tension increases over 50 g, one should increase furnace temperature or reduce draw speed to avoid breaking of fiber. Fabricated fiber is then spooled to a polystyrene drum using drum winder, initially in test band for quality checking before proceeding to the main band. For each fiber pulling session of two hours, at least 100 bar pressure of argon gas is needed. Nitrogen gas is used only in machine pneumatic movements and coating process, thus about 60 bar pressure is enough for a pulling session. After fabrication, the temperature of furnace is set to ramp down. To protect the furnace element, only after the gas valve of furnace turns off automatically, the gas supply, main control cabinet and the other equipment could be shut down accordingly.

3.6 Steps in Fabricating Sunny PCF

3.6.1 Capillaries Fabrication

Capillaries are the basic building blocks for PCFs produced via the stacking method. The quality of capillaries should be given greater attention to ensure structural uniformity of the fabricated PCFs, besides reducing its brittleness and optical attenuation that arise from impurities. Capillaries for stacking are fabricated from undoped high grade silica preform tubes (Heraeus Suprasil F300), drawn to nominal outer diameter of 1-2 mm. Smaller capillary sizes will result in the difficulty of keeping individual capillary in its respective lattice position during stacking process. On the contrary, larger capillary

diameters will lead to lesser rings of air-holes, which increases the confinement loss. To control the size of capillary, preform feeding rate and tractor drawing speed are set according to the simplified mass conservation equation

$$A_f v_f = A_d v_d \tag{4.1}$$

where A_f, A_d are cross-sectional area of preform and capillary respectively, v_f is feeding speed while v_d is drawing speed. It should be noted that this mathematical relation provides only a rough estimation of capillary diameter, careful adjustments of draw speed and temperature is important to achieve the intended size.

Temperature of furnace is maintained between silica softening and melting points, around 2100 ℃. Higher temperature increases surface tension of silica and therefore reduces the ID/OD ratio while the process does not follow the mass conservation equation anymore. Outer diameter of the capillary is measured real-time by the laser diameter gauge. Size uniformity of the capillaries is ensured by enabling automatic feedback system, which is a built-in Proportional Integral Deferential (PID) controller in the draw tower system.

The ID/OD ratio of preform tube is chosen such that the same ratio could be preserved as d/Λ in the resulting PCF, although the d/Λ ratio is dependent on various other factors which will be explained in a later section. Preserving the ID/OD ratio of capillary in drawing process is numerically investigated in (Furusawa, 2003). The collapse ratio is given as

$$C = 1 - \frac{h_1 h_2(0)}{h_2 h_1(0)} \cong \frac{\gamma L}{\mu v_f \ln(v_d/v_f)} \left[\frac{1}{h_1(0)} + \frac{1}{h_2(0)}\right] \tag{4.2}$$

where $h_1(z)$ and $h_2(z)$ are the physical dimensions defined in Figure 3.14. $h_1(0)$ and $h_2(0)$ are the dimensions of the preform tube. L is the furnace's hot zone length and γ is the

surface tension coefficient, estimated as 0.3 N/m. C indicates the extend of capillary collapse with respect to certain parameters. C = 1 indicates complete collapse whereas C = 0 shows the ID/OD ratio is preserved. C is linearly proportional to L and inversely proportional to viscosity μ, draw speed v_d and the dimension of preform tube $h_1(0)$ and $h_2(0)$. As draw speed increases, capillary experiences less heat exposure and lower temperature, thus viscosity increases and the ID/OD ratio maintains. The same scenario happens as the length of hot zone is shortened. Precise control of capillaries dimension and the uniformity are essential in producing a well-ordered PCF preform.

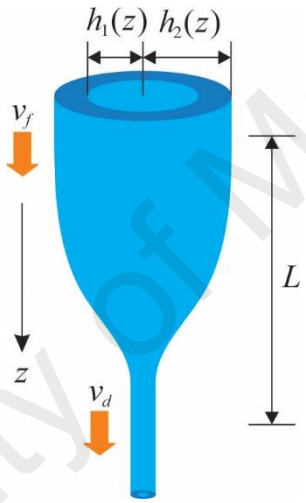

Figure 3.14: Parameter definitions in the model of capillary drawing.

3.6.2 Preform Assembly

Proper stacking is important to form the periodic cladding of PCF. Fabricated capillaries are cleaned and cut into short pieces. Cleaning the capillaries before stacking is vital as contaminants in capillaries will increase PCF scattering loss and reduce its mechanical strength. Dust residue inside PCF preform will burn in high temperature and diffuse into the glass matrix, causing extra losses and fragilities. Capillary surface is cleaned using iso-propyl alcohol or similar type of cleaning agents, while the inner wall of the capillary is cleaned by ultrasonic bath.

Single end of the capillaries are sealed, in this case with high temperature Butanol-fuel hand-torch, to create high pressure inside the capillaries during fiber drawing, effectively preventing PCF holes from collapse. Custom-made hexagonal jigs are used as guides to stack capillaries into triangular lattice arrangement. Capillaries are cut into shorter lengths for easy handling and to avoid disarrangement of freely moving lattice due to bending of long capillaries. Typical cut length of capillaries is 60 cm, shorter cut lengths would be easier to work with, but has the trade-off of lesser fabricated PCFs.

Stacking is done with all the sealed ends facing one direction. Using the hexagonal jigs, capillaries are initially stacked inside a suitable jacketing tube which is shorter than the capillaries. The center capillary is replaced with a rod of the same size as the other capillaries, creating the core of PCF. To obtain the Sunny PCF preform, at the sealed side, the first ring of capillaries is sealed together with the rod, retaining the interstitial holes around the core in Sunny PCF forming sunny structure. The hexagonal shape of the capillaries stacking is fixed by paper tapes, then the jigs are released. Voids at the six hexagonal sides are filled tightly with packing rods of different sizes, which are cut shorter to avoid compressing and breaking of the bulging sealed ends. Subsequently, the stacking is transferred slowly into a longer preform tube. Finally, to prevent capillaries from falling out, a metal stop is attached to the end of Sunny PCF preform where capillaries ends are open. The last step is necessary if the preform is not heat-treated in a lathe to hold the capillaries firmly prior to pulling.

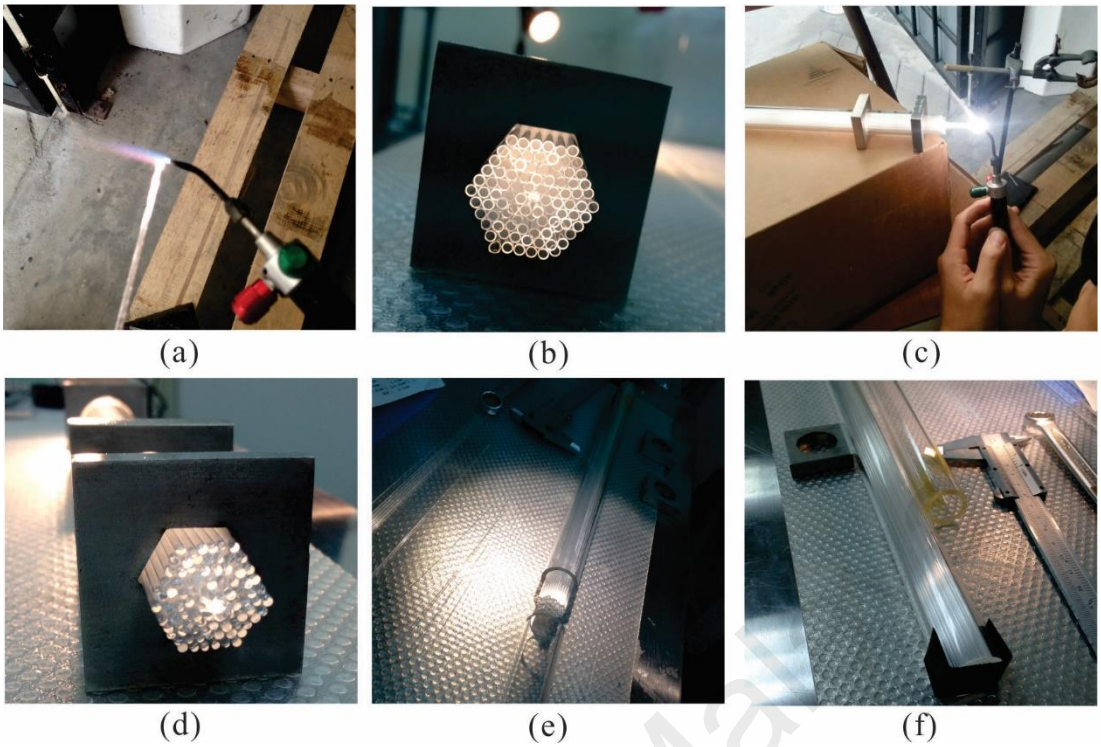

Figure 3.15: Sunny PCF preform assembly: (a) end sealing; (b) stacking; (c) creating sunny structure; (d) sealed side of the stacking; (e) jacketing; (f) Sunny PCF preform.

3.6.3 Drawing

Drawing of Sunny PCF involves two stages, caning and fiber pulling. In the first stage, PCF preform is drawn to some 1-2 mm canes. Initial feeding rate and drawing speed are set according to the mass conservation equation. During the process, drawing speed is adjusted slowly to reach the intended dimension of canes. Temperature of furnace is set in the range of 1950-2050 ℃. Temperature above 2050 ℃ will result in complete collapse of air holes or irregular hole shapes due to low viscosity and surface tension whereas temperatures lower than 1950 ℃ may lead to random cracks and interstitial holes. The optimum temperature is found to be within 10 ℃ around 2020 ℃. Interstitial holes except those in the sealed first ring capillaries are closed by applying 20 kPa of vacuum pressure inside the preform.

Slow draw speed of about 1 m/min is used since ensuring complete collapse of interstitial holes is more important than reducing brittleness in the first stage. Cross-

sectional surface of cane samples are observed under microscope from time to time to make sure the formation of uniform lattice pattern. Meanwhile, temperature of furnace is adjusted carefully in steps of 5 ℃ depending on the observed cross-sectional surface of samples. Ovality of sample is monitored closely as it indicates deformation of samples due to trapped air or the existence of non-uniform pressure in capillaries.

In the second stage, one end of Sunny PCF cane is sealed using butane-fuel hand torch and inserted into a suitable silica cladding tube. The choice of cladding tube depends on the intended final scaling of the microstructure. Using a smaller ID/OD ratio cladding tube will result in smaller d, d/Λ and vice versa. Before second stage drawing, it is crucial to heat the cane in the furnace at 1600 ℃ for a few quick passes, aiming to create homogenous temperature environment in all air holes, so that the fabricated Sunny PCF has uniform microstructure along the fiber (Tse, 2007). The principle of drawing of cane to fiber is similar to the first stage, with judicious control of drawing speed, temperature and pressure. Vacuum is applied inside the cladding tube so as atmosphere pressure will force the gap between Sunny PCF cane and cladding tube to melt and close in furnace. Temperature of furnace is increased slightly to close the interstitial holes if they remain in the caning process.

When the process is stable, polymer coating is applied to the fabricated Sunny PCF, coated Sunny PCF is then wind into a large spool using drum winder. To improve the mechanical strength of PCF, tension is maintained below 50 g by controlling furnace temperature and the draw speed is increased to more than 4 m/min.

3.6.4 Fabricated Sunny PCF

Sunny PCF with a continuous length of 30 m has been fabricated, measuring 126 μm in diameter without coating. The cross-sectional of the Sunny PCF is shown in Figure

3.16. The uniformity of the microstructure has been confirmed by comparing several microscope images taken at different length.

Fabrication of MOF is a challenge. A slight mistake in any step will result in a defective MOF. Since air is a poor heat conducting medium, without pre-heating, temperature is not spread evenly in the preform or cane, the air in each hole will experience different temperature which gives rise to non-uniform air hole pressure during draw process, where some holes will expand more quickly and some collapse entirely. Another important issue is the packing rod arrangement during preform stacking. Loose arrangement in packing rods causes the existence of interstitial holes at the outset ring.

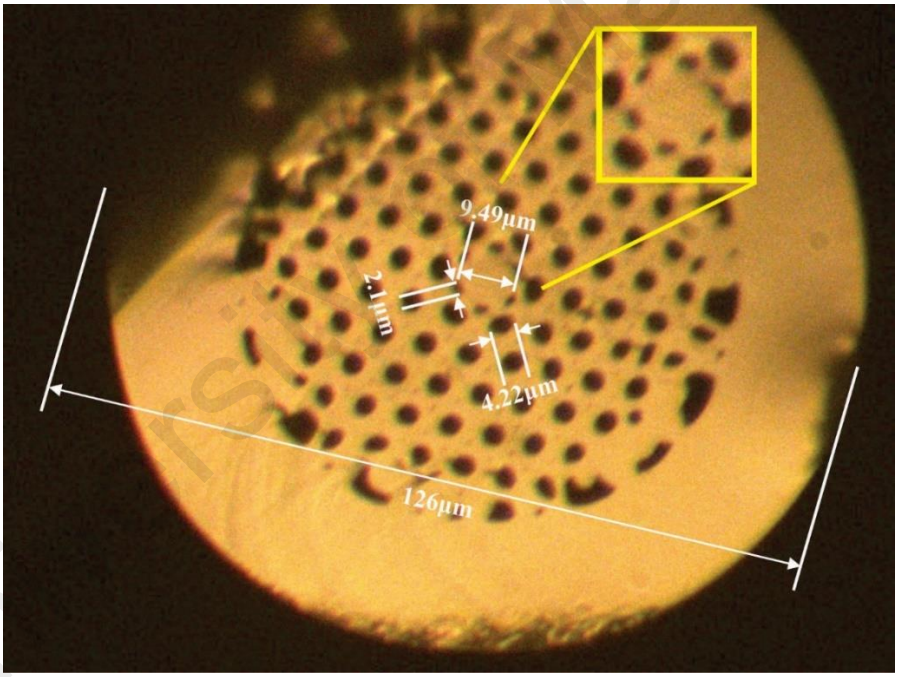

Figure 3.16: Microscope image of a preliminary Sunny PCF fabricated using stack-and-draw technique.

Still, the feasibility of sunny structure has been successfully demonstrated here. This is the crucial part in Sunny PCF which is providing a high evanescent field exposed light-matter interaction medium. By paying extra attention on the aforementioned issues, an ideal Sunny PCF can be fabricated using stack-and-draw method.

3.7 Conclusion

For every d/Λ, Sunny PCF provides higher evanescent field exposure as compared to conventional PCF. The proposed sunny structure can boost up the highest achievable evanescent field exposure in a conventional PCF from 15.83% to 21.23% with $d/\Lambda = 0.9$ with negligible confinement loss. At the operating wavelength of 1550 nm, suspended-core holey fiber (formerly known as the best candidate for evanescent field exposure) with core diameter of 1.2 μm achieves evanescent field exposure of 11.5% with the confinement loss of 0.29 dB/m. Sunny PCF with larger core diameter of 1.33 μm can achieve the same evanescent field exposure as suspended-core holey fiber with much lower confinement loss, which is a good finding. From the microscope image of the fabricated Sunny PCF, the feasibility of obtaining sunny structure by sealing the first ring of capillaries together with the core during preform preparation has been confirmed.

CHAPTER 4: DIAMOND RING FIBER

4.1 Design of DRF

Besides high evanescent field exposure, some sensing applications do require material coating to realize their respective sensing mechanism. Optical biosensors, for example, require a metal/dielectric interface for SPR to occur. Hence, to be a better MOF in sensing applications, large cavities should be there for ease of material coating process. A novel MOF which is able to fulfill all the good criterion mentioned so far has been proposed (Ng, Wong, et al., 2017), named Diamond Ring Fiber (DRF).

The proposed DRF, shown in Figure 4.1, is an all-silica optical fiber. The structure is mainly formed by a micro-scaled silica core and a fiber-size capillary shield to realize the concept of a protected microfiber which is able to provide a durable and enclosed light-matter interaction medium. The micro-scaled silica core acts as a microfiber which allows high evanescent field exposure with low confinement loss. The silica core is located in the middle of the capillary shield in order to minimize coupling loss with conventional optical fibers.

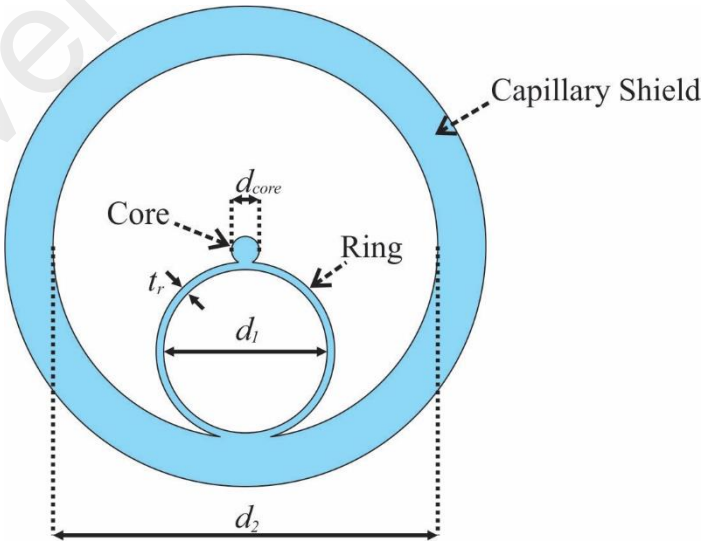

Figure 4.1: Cross-sectional view of the proposed DRF

DRF is designed to be fabricated using stack-and-draw fiber drawing technique in order to be a high quality long length fiber. The best method to create a center point in a jacket glass tube is by stacking three capillaries as shown in Figure 4.2 with the dimension calculated from the following equation

$$d = \frac{D}{1+2/\sqrt{3}} \tag{5.1}$$

where D is the inner diameter of the jacket glass tube and d is the outer diameter of each capillary in the DRF preform. Detailed fabrication process will be covered in next section where only one capillary will be retained as the ring in DRF to support the core which will give a higher air-filling ratio. Air-filling ratio tells the percentage of hollow space in a silica structure. This design, at the same time, creates two cavities which are relatively large compared to the existing microstructured fibers. The physical design parameters of the DRF are d_{core} that is the diameter of the core, d_1 is the inner diameter of the ring, d_2 is the inner diameter of the shield and t_r is the thickness of the ring. For the light to propagate inside the core, t_r has to be smaller than d_{core}. Hence, a detailed calculation for selecting the jacket glass tube and capillaries in the preform stacking stage is required.

4.2 Fabrication

Two glass tubes with different wall thickness have been used for fabricating the DRF, one with inner to outer diameter of 17.5mm/25mm and the thinner one measuring 18mm/20mm. The thicker glass tube is used as the jacket tube while the thin tube is drawn into capillaries with smaller outer diameter of 8.12 mm. Three capillaries are then stacked inside the jacket tube and a silica rod is inserted in the central space between them as the DRF core as shown in Figure 4.2. Two capillaries stacked at the beginning and end part of the jacket tube are in short length, used for the purpose of holding and positioning of the central core during fiber drawing process. The long capillary stacked in the jacket is meant to be joined with the central core along the fiber length.

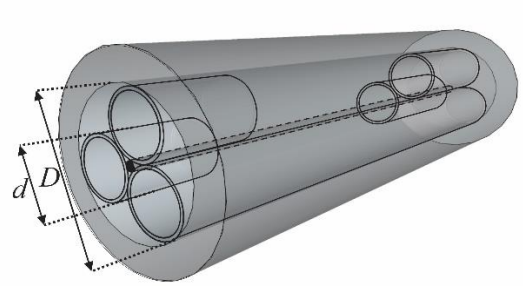

Figure 4.2: Schematic view of the DRF preform. The central silica rod indicates the fiber core for light guiding.

Prior to pulling, the DRF preform is annealed at 1800 ℃ to introduce a mild surface joining between the long capillary and the central rod. Then, the preform is pulled based on the conservation of mass equation to determine pulling parameters such as preform feed and drawing rates to produce the desired output diameter. The preform is drawn into cane measuring 1mm in diameter at a temperature of 1930 ℃ with drawing speed of 1.6 m/min. The structure, particularly the core position, is carefully controlled by controlling the applied pressure into the long capillary. The fabricated cane structure is frequently checked under microscope throughout the whole drawing process. The first few meters of the cane are discarded because these canes are with 3 rings structure resulting from the short supporting capillaries in the initial part of the preform.

The DRF cane is then pulled into fiber form measuring 125 μm in diameter at a temperature of 1820 ℃ and 0.5 m/min draw speed. The diameter of the DRF is chosen to be 125 μm for easier splicing with the standard SMF. The scanning electron microscope (SEM) (Hitachi Tabletop Electron Microscope TM3030) image of the fabricated DRF is shown in Figure 4.3. The fabricated DRF is the same as the desired structure with measured parameters of d_{core} = 6.68 μm, d_1 = 35.1 μm, d_2 = 90.2 μm, and t_r = 2.51 μm. To date, with the d_2 size as large as 90.2μm, DRF is providing the largest cavity among reported microstructured fibers (Cordeiro et al., 2006; Euser et al., 2008; Fini, 2004;

Olyaee et al., 2014; Park et al., 2011; Webb et al., 2007; Yu et al., 2008; Zhi-guo et al., 2008).

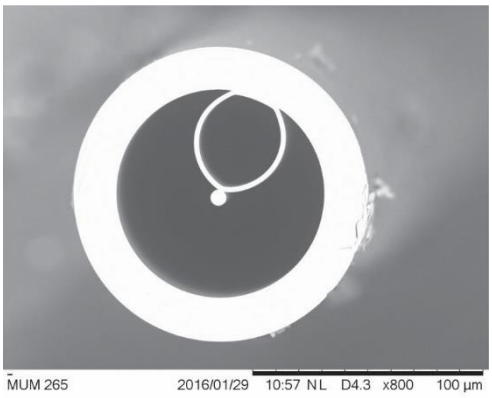

Figure 4.3: SEM image of the fabricated DRF.

In order to show the flexibility to fabricate DRF with different parameters and core sizes, DRF cane is pulled with two steps of jacketing called as single and double jacket. A single jacketed cane is formed by inserting a 1 mm DRF cane into a capillary with slightly larger inner diameter, while the double jacketed cane is formed by inserting a DRF cane into two consecutive larger capillaries as shown in Figure 4.4.

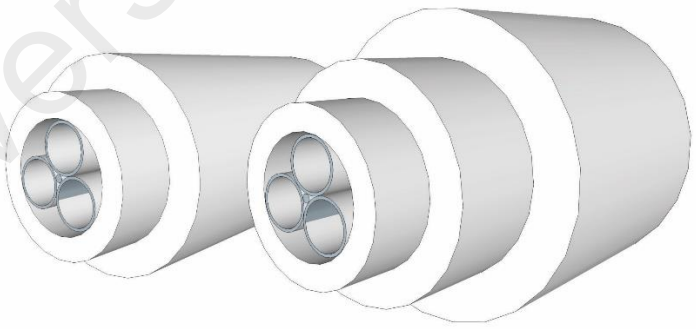

Figure 4.4: Single jacketed cane (left) and double jacketed cane (right).

The single and double jacketed DRF canes are then pulled into standard fiber size of 125 µm, aiming the higher order jacketed cane to produce a DRF fiber with smaller core. For these fabrications, the head of 1 mm cane is fused for self-pressurization, while a vacuum pressure is applied from the top of the preform to collapse the jacket(s) with the

DRF cane during the drawing process. The jacketed canes are pulled into fiber size with drawing speed of around 1.5 m/min and temperature of around 1850 ℃. Figure 4.5 shows the SEM images of the fabricated single jacketed DRF and double jacketed DRF. Based on the SEM images, the waveguide parameters have been scaled down to d_{core} of 4.96 μm, d_1 of 29.5 μm, d_2 of 62.8 μm, and t_r of 1.45 μm in the single jacketed DRF and further reduced to d_{core} of 3.23 μm, d_1 of 21.36 μm, d_2 of 46 μm, and t_r of 0.94 μm in the double jacketed DRF. These measurements prove that fabrication of DRF with different parameters is possible. The smallest core size that we have successfully fabricated is 1.5 μm.

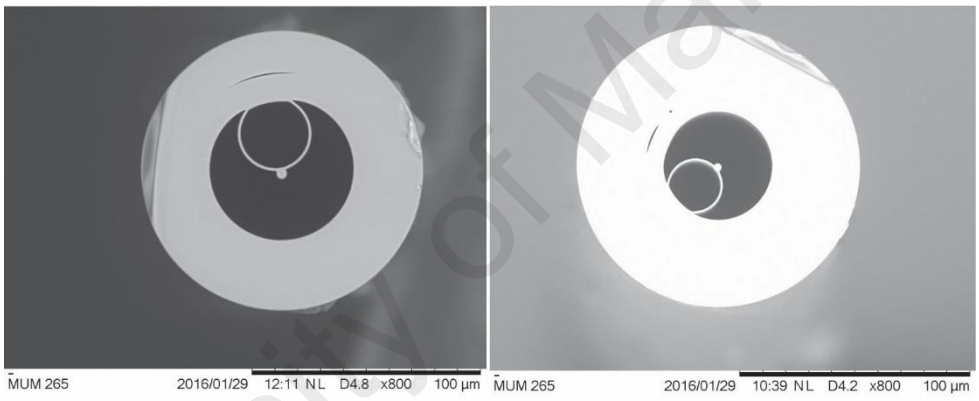

Figure 4.5: Single jacketed DRF (left) and double jacketed DRF (right).

4.3 Characterization

Figure 4.6 shows the experimental setup for mode analysis of the fabricated DRFs. In this setup, a laser source (WSL-100, Santec) operating at 1550 nm wavelength is used to launch light into one meter long DRF coupled via SMF. Both DRF and SMF are aligned through butt coupling. The output from the DRF is collimated by using an objective lens (M-20X, Newport) and directed to a beam splitter (FW1, Thorlabs) to split the output equally into charge-coupled device (CCD) (7290A, Electrophysics) and beam profiler (BP109-IR, Thorlabs). The experiment is then repeated by changing the fiber under test to single jacketed DRF and double jacketed DRF.

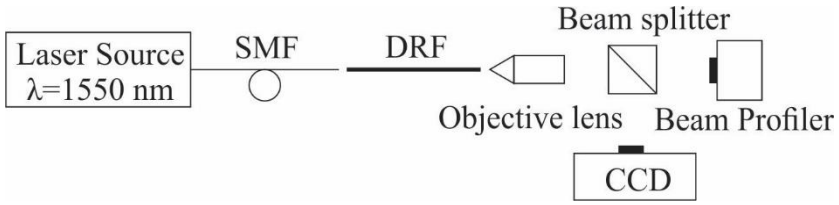

Figure 4.6: Experiment setup for analyzing guided mode in DRFs.

The captured CCD images from the experiment show the power distribution of the guided mode in each fabricated DRFs as depicted in Figure 4.7. The intense spot shows the guided mode in the silica core. In DRF, small fraction of the light penetrates into the ring. This is due to the thickness of the ring which is relatively thick compared to the wavelength of the light. The reduced ring thickness in single jacketed DRF decreases the penetration of light into the ring. In double jacketed DRF, the light is well guided inside the core.

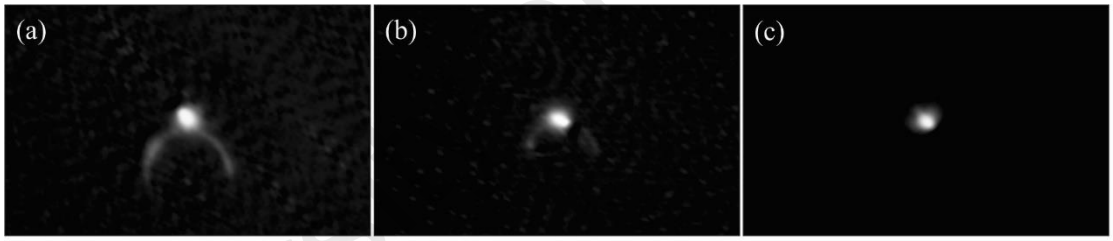

Figure 4.7: CCD images of the guided mode in (a) DRF, (b) single jacketed DRF and (c) double jacketed DRF.

One-dimensional mode intensity profile is obtained for each DRF using beam profiler and shown in Figure 4.8. In horizontal axis, DRFs show symmetrical mode profiles due to the symmetrical step-index profile. In vertical axis, the step-index profile is air-silica-silica-air, which is asymmetrical due to the fact that silica contributed by the ring is relatively thin. However, double jacketed DRF is able to show symmetrical mode profile in horizontal axis since the ring thickness reaches the diffractive limit (H. W. Lee, 2012) of the silica.

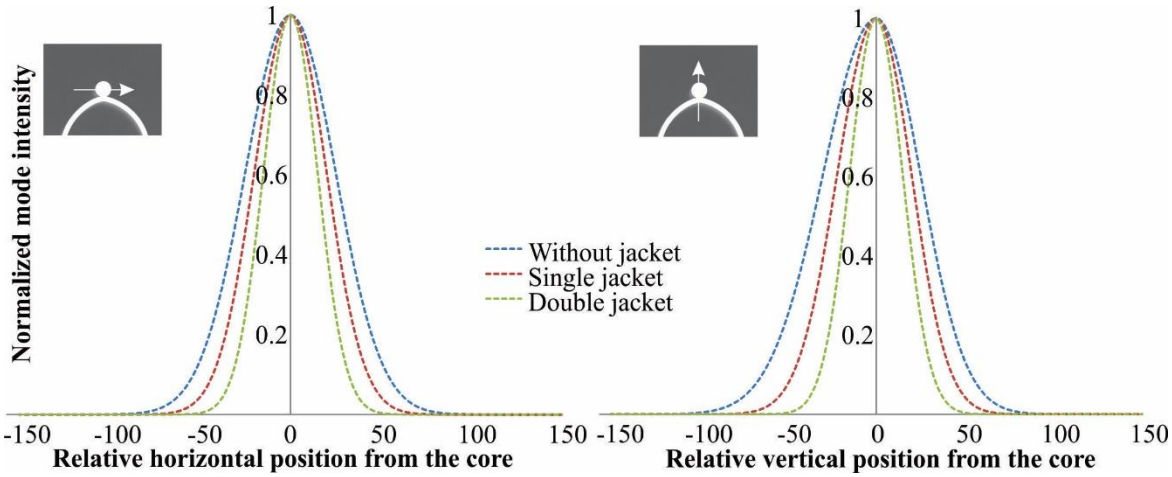

Figure 4.8: Mode intensity profile obtained using beam profiler.

The guiding ability of DRFs has been confirmed here. In fact, propagation loss and coupling loss of the DRFs can be characterized using cut-back technique. The loss versus length graph in cut-back method can tell the propagation loss and coupling loss via gradient and the intersection between graph and *y*-axis. However, it is not carried out since this work is mainly focus on design, simulation and fabrication. Furthermore, the fabricated DRFs are uncoated and fragile, causing difficulties in cutting and handling of a 100 long fiber.

4.4 Simulation

The simulation of the diamond ring fiber is done by using commercially available finite element method software, COMSOL MULTIPHYSICS^{TM} to solve the Maxwell's equations. The SEM images of the DRFs are imported into the software to simulate the exact fabricated structures for comparison with the experimental results, as shown in Figure 4.9. In addition, PML is added surrounding the structure to attenuate and absorb the outward propagating electromagnetic wave from being reflected back into the simulation region.

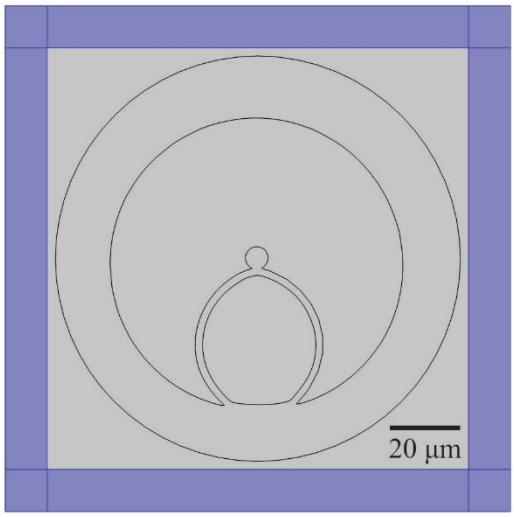

Figure 4.9: FEM model using SEM image of fabricated sample. The highlighted area indicates PML.

The refractive index of silica, n_{silica} is set according to the operating wavelength λ using Sellmeier equation (Tatian, 1984). DRF, single jacketed DRF and double jacketed DRF are simulated at a wavelength of 1550nm. In addition to the 3 different core sizes, DRFs with other different core sizes (by scaling down the SEM image of DRF) are simulated to study their performance in terms of evanescent field exposure and confinement loss.

While scaling down the structure of DRF, the core size is getting smaller. When the core size is larger than the λ, only the guided mode protrudes into the surrounding medium, which is the air. Smaller core size can expose more evanescent field to the air cavities. Figure 4.10 shows the relationship among evanescent field exposure, confinement loss and the core size of a DRF. Reaching the condition where core size is near to or smaller than λ, evanescent field exposure starts to increase tremendously. In our simulation, we stop at the core size of 0.8 μm because significant increase in the confinement loss due the diffraction limit of the silica is noticed. Using the DRF structure, highest achievable evanescent field exposure is 39.56% with the negligible confinement loss of <0.025 dB/m, at 1550 nm wavelength and 0.8 μm core size. Low confinement loss

is important to further enhance the sensing performance by allowing longer interaction path between the light and matter.

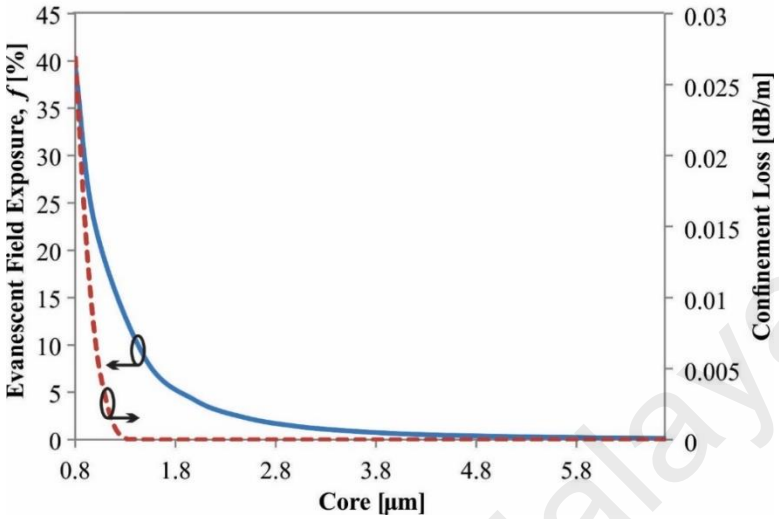

Figure 4.10: Relationship among evanescent field exposure, confinement loss and core size of a DRF.

Figure 4.11 shows the dependence of evanescent field exposure and confinement loss to λ, at the core size of 0.8 μm. For λ smaller than 1550 nm, evanescent field exposure increases at higher λ, due to higher penetration of guided mode into the air cavities. When the λ is getting higher than 1550 nm, both the evanescent field exposure and confinement loss increase excessively since the light is no longer well guided inside the relatively smaller core size. For any application which requires smaller λ, high evanescent field exposure can still be obtained using DRF with the core size smaller than 0.8 μm without introducing significant confinement loss.

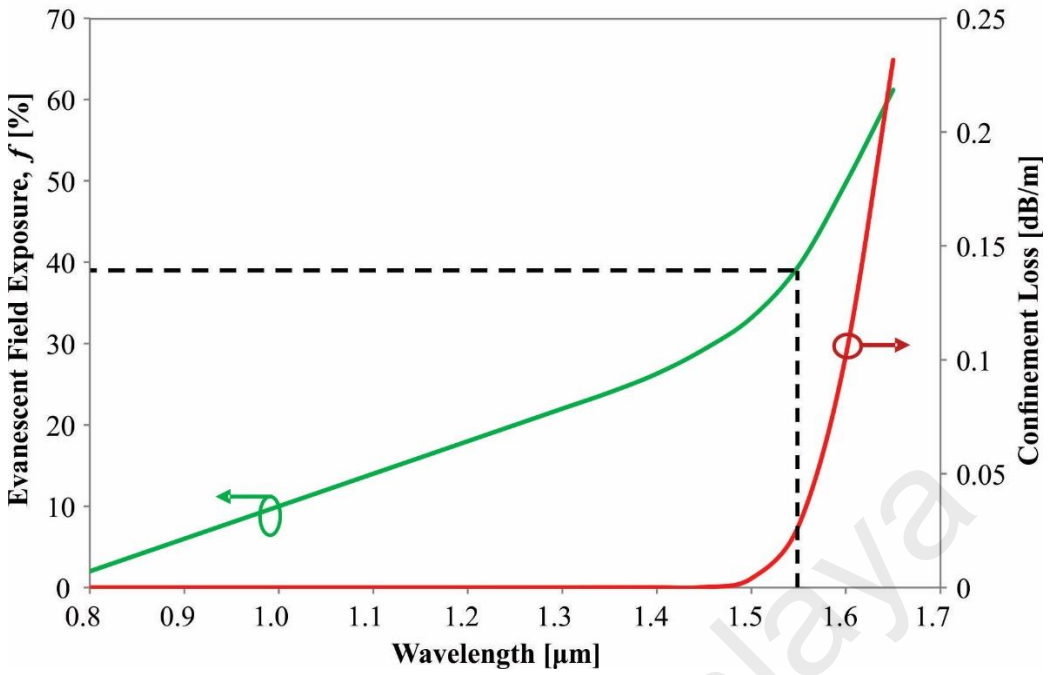

Figure 4.11: Dependence of evanescent field exposure, *f* and confinement loss to the wavelength at the core size of 0.8 µm.

DRF which provides the aforementioned highest achievable evanescent field exposure is consisting of a protected nanofiber measuring 0.8 µm in diameter and two cavities with the diameter of 4.2 µm and 10.8 µm respectively. The average cavity size in the reported suspended-core holey fiber (Webb et al., 2007) is around 3.6 µm. At the same core size of 0.8 µm DRF is capable to deliver much higher evanescent field exposure while providing larger cavities for ease of material coating as well as infiltration of liquids and gases.

4.5 DRF based Surface Plasmon Resonance (SPR) Sensor

SPR sensor attracts much attention since last few decades due to its high sensitive nature and broad range of sensing applications such as medical diagnostics, biomolecular analytes detection, antibody-antigen interaction and etc. (Homola, 2003; Rifat et al., 2016; Wong, Krupin, Sekaran, Mahamd Adikan, & Berini, 2014). SPR refers to the resonant oscillation of free electrons of metal and electromagnetic fields due to incident light in a metal-dielectric interface.

In 1983, Liedberg *et al.* (Liedberg, Nylander, & Lunström, 1983) reported the first prism SPR technique for biosensing and gas detection. The prism based SPR sensor does give robust performance. However, its bulky structural configuration resulting from the optical and mechanical components is not convenient for remote sensing (Rifat et al., 2016; Robinson, 1995). To overcome the prism-SPR sensor limitations, PCF based SPR sensors have been proposed. PCF is compact and miniature in size which benefits the SPR sensing applications. Besides the SPR sensing, fiber or waveguide based refractive index (RI) sensing techniques such as fiber Bragg grating (FBG), modal interferometer, long period fiber grating (LPFG) and micro-ring resonator based sensing have been proposed (Ahmed et al., 2016; Iadicicco, Cusano, Cutolo, Bernini, & Giordano, 2004; Rao & Zhu, 2007; Zhao, Cai, Li, Meng, & Zhao, 2014; Zhao, Li, Cai, & Yang, 2015). However, only a very narrow wavelength shift will be shown by these sensors against the changes in analyte's RI. On the contrary, SPR sensor provides high sensitivity by showing large resonance wavelength shift even against a very small RI difference. The first optical fiber SPR sensor has been demonstrated by Jorgenson (Jorgenson & Yee, 1993) in 1993. Following that, various PCF SPR sensors have been proposed to improve the SPR sensing performance. In 2006, Hassani *et al.* reported the microstructured optical fiber based SPR sensor for the first time (Hassani & Skorobogatiy, 2006). Recently, PCF SPR sensors with inside metal coating and selective liquid infiltration into the air holes have been studied (An et al., 2017; Dash & Jha, 2014; Gao, Guan, Wen, Zhong, & Yuan, 2014; A. A. Rifat et al., 2015; Shuai, Xia, & Liu, 2012; F. Wang, Sun, Liu, Sun, & Chu, 2016). However, their practical implementation are very challenging, especially the process to infiltrate liquid selectively into small air holes. To overcome the limitations, D-shaped PCF SPR sensors have been introduced (Dash & Jha, 2015; Tian, Lu, Chen, Lv, & Liu, 2012), where metallic layer and analyte layer are directly applied onto the flat top surface of D-shaped PCF. Nonetheless, this requires extra effort on accurate polishing to remove

the predetermined portion of PCF. In other studies, outside metal deposition and sensing layer formation have been proposed with irregular PCF structures (Hameed, Alrayk, Shaalan, El Deeb, & Obayya, 2016; Otupiri et al., 2014; A. Rifat et al., 2015). Outside sensing layer formation paves a simple sensing process. However, due to the irregular geometry of the microstructure optical fiber, fabrication of such fiber is challenging. Also, structures with outer coating are environmentally sensitive and require extra precaution in handling. Experimental study of PCF based SPR sensors are yet to be explored in a large scale due to the complexity of reported fiber structures.

The preferred method for depositing semiconductors and metals, including nearly all of the technologically important semiconductors, is chemical vapor deposition (CVD). However, CVD onto the walls of the long, extremely narrow pores in a PCF presents two challenges: small deviation from perfect conformal deposition, and mass transport of the reactants into and by-products out of such a confined space is prohibitively slow using traditional techniques. High-pressure microfluidic chemical deposition has been reported in the fabrication of high-quality polycrystalline and single-crystal semiconductors within the voids of PCFs (Boehm, Fran ̧ois, Ebendorff-Heidepriem, & Monro, 2011; Sazio et al., 2006). High-pressure flow, which can be sustained because of the very high mechanical strength of optical fibers, overcomes mass-transport constraints and also enables a strikingly uniform, dense, and conformal annular deposition onto the capillary walls, even for pores that reduce to less than 10 nm in diameter. DRF proposed earlier in this work provides relatively large cavities as compared to those reported PCFs which eases the metal coating process. Hence, DRF has been studied on its application as a SPR sensor (Ng, Rifat, Wong, Mahdiraji, & Adikan, 2017). Apart from the advantage of having large cavities, DRF SPR sensor does not require selective infiltration of analyte. In the following sections, DRF will be discussed on its application as a SPR sensor.

4.6 Structural Design and Theoretical Modeling

Cross-sectional view of the proposed DRF SPR sensor is shown in Figure 4.12. DRF is an all-silica fiber which is having a ring capillary with the thickness, t_r = 0.94 μm to support the core in the middle along the fiber. The core size of the fiber, d_{core} is measuring at 3.23 μm. Gold metal layer with the thickness, t_{gold} = 50 nm is coated on the inner wall of the ring capillary. Analyte is infiltrated into both of the DRF's cavities, small one with the diameter, d_1 = 21.36 μm and the large one with the diameter, d_2 = 46 μm.

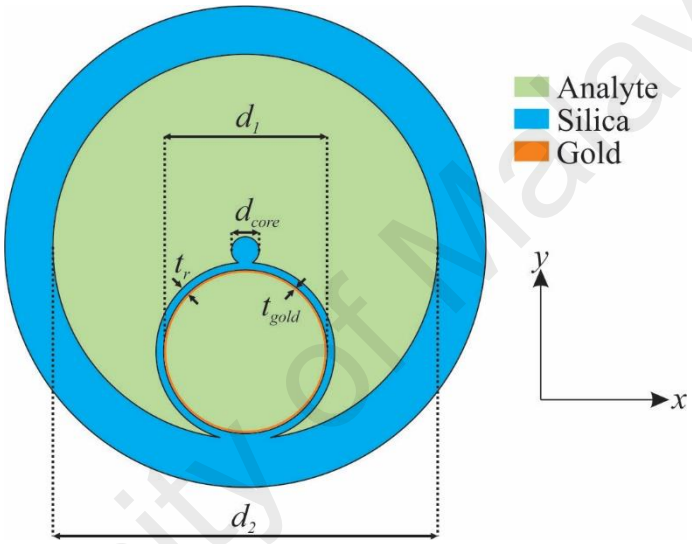

Figure 4.12: Cross-section of the proposed sensor.

The refractive index of silica, n_{silica} is obtained according to the operating wavelength, λ following Sellmeier equation (Tatian, 1984). The dielectric constant of gold is determined by using the Drude-Lorentz model (Vial, Grimault, Mac ás, Barchiesi, & de La Chapelle, 2005) with the equation

$$\varepsilon_{Au} = \varepsilon_{\infty} - \frac{{\omega_D}^2}{\omega(\omega + j\gamma_D)} - \frac{\Delta\varepsilon.{\Omega_L}^2}{({\omega^2 - \Omega_L}^2) + j\Gamma_L\omega} \qquad (6.1)$$

where ε_{Au} is the permittivity of the gold material and ε_{∞} is the permittivity at high frequency with the value of 5.9673. ω is the angular frequency which can be expressed as $\omega = 2\pi c/\lambda$ where c is the velocity of light in vacuum. ω_D is the plasma frequency in

which $\omega_D/2\pi$ = 2113.6 THz whereas γ_D is the damping frequency in which $\gamma_D/2\pi$ = 15.92 THz. The value of the weighting factor, $\Delta\varepsilon$ is 1.09. Spectral width and oscillator strength of the Lorentz oscillators are expressed as $\Gamma_L/2\pi$ = 104.86 THz and $\Omega_L/2\pi$ = 650.07 THz respectively.

COMSOL MULTIPHYSICS™ software is used to investigate the light guiding properties and sensing performances of the proposed sensor. The circular PML boundary condition has been considered to absorb the scattered light towards the surface.

The possible experiment setup for DRF SPR sensor is demonstrated in Figure 4.13. Supercontinuum laser source could be used to launch the incident light into the sensor via single-mode polarization-maintaining fiber (PMF) and aligned to the sensor through butt-coupling. The output from the sensor will be analyzed by the optical spectrum analyzer (OSA).

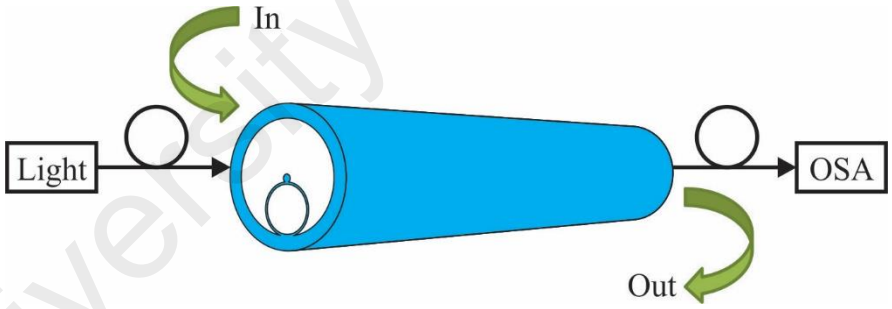

Figure 4.13: Schematic diagram of the experimental set-up.

4.7 Results and Discussion

DRF SPR sensor is working based on the principle of interaction between evanescent field and the gold layer. Evanescent field produced from the core guided light penetrates into the air cavity where the gold layer is coated. Resonance will occur while the real part of n_{eff} of the core guided mode and surface plasmon polaritons (SPP) mode is mathematically identical. Core-guided mode is coupled to the SPP mode at a resonance condition which is called the phase matching point and produces a sharp loss peak.

Figure 4.14 shows the phase-matching condition of the proposed sensor. As shown in Figure 4.14a, the sensor shows higher resonance loss peak using *y*-polarized fundamental mode as compared to that of *x*-polarized fundamental mode. Figures 4.14b and 4.14c show the *y*-polarized core mode and *x*-polarized core mode, respectively. Obviously the *y*-component electric field is stronger in the sensing layer due to the fact that it is refracted towards the metal surface. Hence, for the remainder this work, *y*-polarized light is considered. Figure 4.14d shows the SPP mode on the surface of the metal. With the analyte's RI of 1.33, phase matching was found at λ = 620 nm where the dispersion relations of core guided mode and SPP mode intersects and resonance peak loss occurs. The confinement loss was calculated by

$$\alpha[\mathrm{dB/cm}] = 8.686 \times \frac{2\pi}{\lambda} \mathrm{Im}[n_{eff}] \times 10^4 \qquad (6.2)$$

where Im[n_{eff}] is the imaginary part of the effective mode index and λ is expressed in the unit of μm. Largest energy is transferred to SPP mode from the core guided mode at this phase-matching point. Both of the modes are strongly coupled as shown in Figure 4.14e.

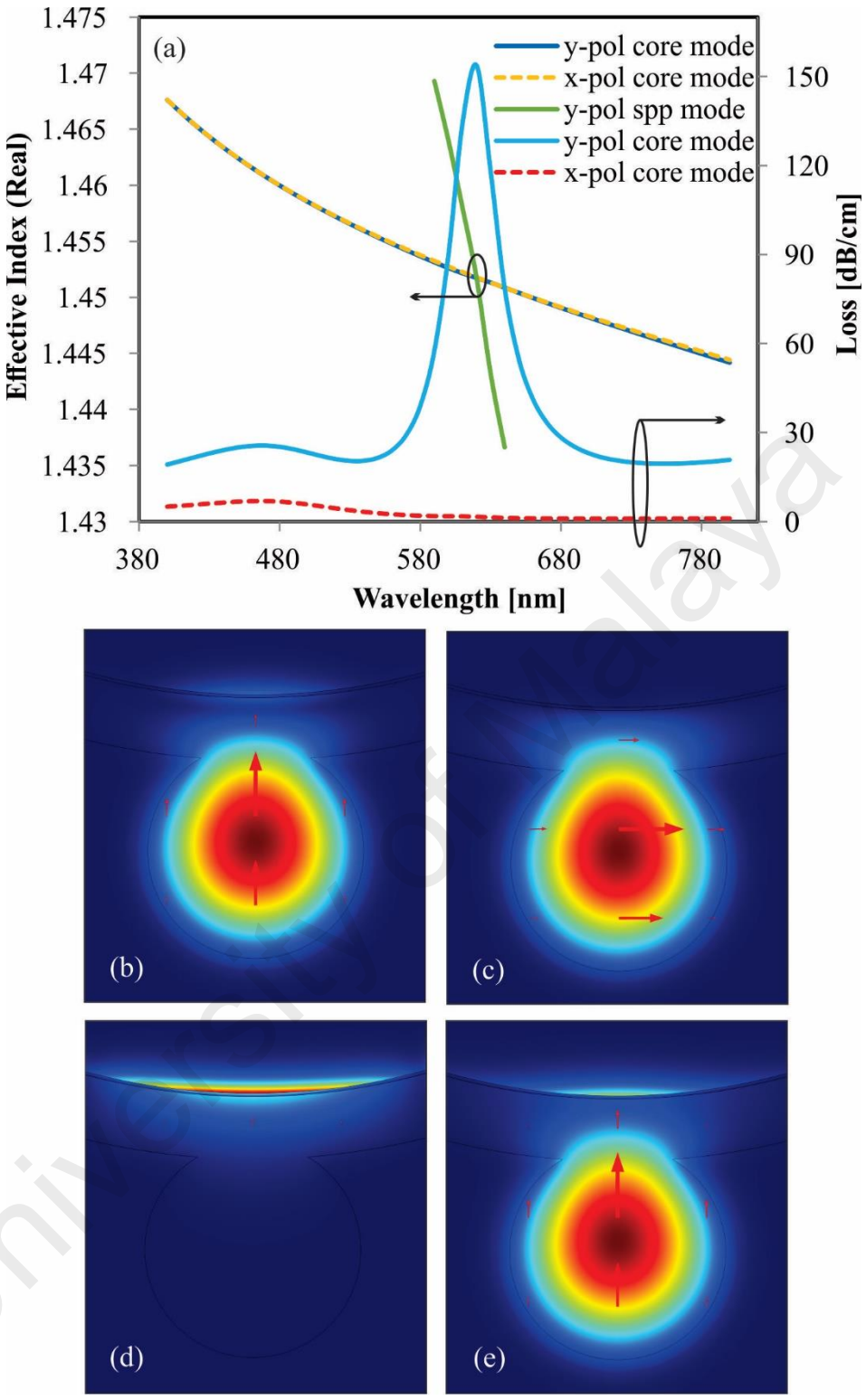

Figure 4.14: (a) Dispersion relations of core guided modes and SPP mode with analyte's RI of 1.33. Electric field distributions of the (b) *y*-polarized core mode, (c) *x*-polarized core mode, (d) *y*-polarized plasmon mode at λ = 580 nm; and (e) *y*-polarized core mode at λ = 620 nm (phase matching point).

Real part in the effective refractive index of the SPP mode is strongly affected by the RI of analyte, resulting in the change of phase-matching wavelength with a small change

in analyte's RI. Figure 4.15 shows the effect of analyte RI on the loss spectrum. Increasing analyte RI will shift the SPP curve in Figure 4.14a towards higher value collectively. This shifts the resonance peak loss towards longer wavelength. The increase in analyte's RI also decreases the core-cladding index contrast which leads to higher light penetration to the cladding region. Hence, loss depth is increasing with the higher analyte RI. A minimum propagation loss of 154 dB/cm is achieved at n_a = 1.33 while the maximum propagation loss is 548 dB/cm at n_a = 1.39.

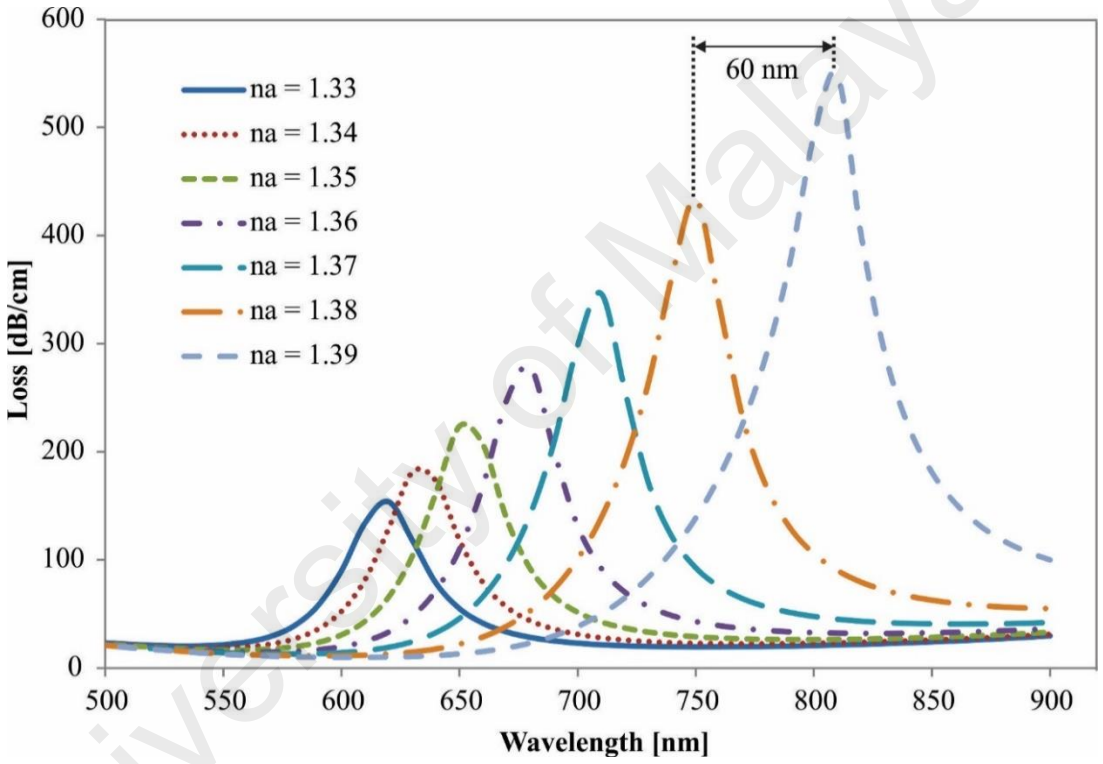

Figure 4.15: Fundamental loss spectrum.

A maximum resonance wavelength shift from 750 nm to 810 nm (60 nm) is found when the analyte RI is varied from 1.38 to 1.39. This allows the proposed sensor to have a maximum wavelength sensitivity of 6000 nm/RIU, which is higher than the reported PCF SPR sensors (An et al., 2017; Dash & Jha, 2014; A. A. Rifat et al., 2015). It also shows the sensor resolution of 1.67×10^{-5} RIU (by assuming minimum spectral resolution of 0.1 nm). Wavelength interrogation sensitivity is determined by

$$S_\lambda(\lambda) = \frac{\Delta\lambda_{peak}}{\Delta n_a} \tag{6.3}$$

where $\Delta\lambda_{peak}$ is the peak shift and Δn_a is the variation in analyte's RI. For the analyte's RI of 1.33, 1.34, 1.35, 1.36, 1.37 and 1.38, the resonance loss peaks are found at the wavelength of 620, 630, 650, 680, 710 and 750 nm, respectively. This indicates that the wavelength sensitivities of 1000, 2000, 3000, 3000 and 4000 nm/RIU are achieved when the changes in analyte RI are 1.33-1.34, 1.34-1.35, 1.35-1.36, 1.36-1.37 and 1.37-1.38, respectively. The proposed sensor shows an average wavelength sensitivity of 3107 nm/RIU; and the polynomial regression of resonant wavelength R^2 is 0.9987, which indicates the good fitting of the sensing performance (Figure 4.16). For the practical detection of analytes, self-calibration is needed with respect to RI range.

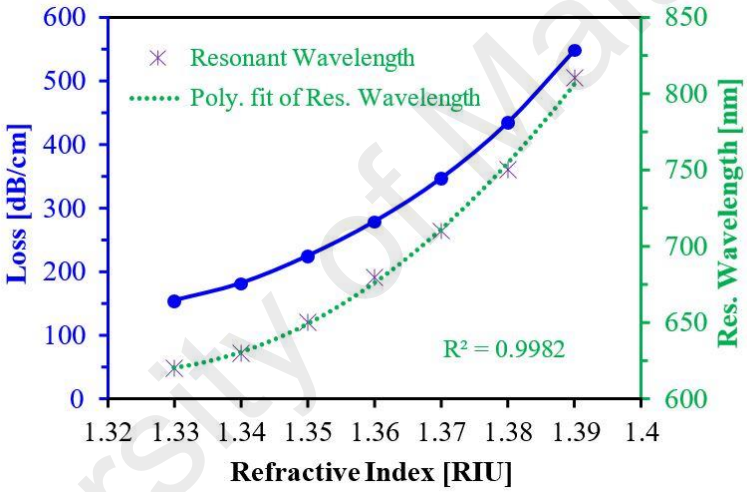

Figure 4.16: Linear fit of the resonant wavelength with varying analyte RI from 1.33 to 1.39 (with iteration of 0.01).

Compared to wavelength interrogation method, amplitude interrogation method is easier and cost effective since it requires measurement only at a specific wavelength (A. A. Rifat et al., 2015). The disadvantage is a smaller dynamic range and lower sensitivity when compared to the wavelength interrogation approach, in which the whole transmission spectra are taken and compared before and after the change in the analyte has occurred. Amplitude interrogation sensitivity is obtained from

$$S_A(\lambda)[\mathrm{RIU}^{-1}] = -\frac{1}{\alpha(\lambda,n_a)}\frac{\partial\alpha(\lambda,n_a)}{\partial n_a} \tag{6.4}$$

where $\partial\alpha(\lambda, n_a)$ is the difference in power at a specific wavelength caused by the small change in analyte's RI, ∂n_a and $\alpha(\lambda, n_a)$ is the overall loss. Increasing in analyte's RI increases the amplitude sensitivity as shown in Figure 4.17 due to the higher interaction between the evanescent field and SPP mode. The proposed sensor shows the maximum amplitude sensitivity of 508 RIU^{-1} at analyte RI of 1.38, which is comparable to reported works (Gao et al., 2014; A. A. Rifat et al., 2015), with simple sensor structure.

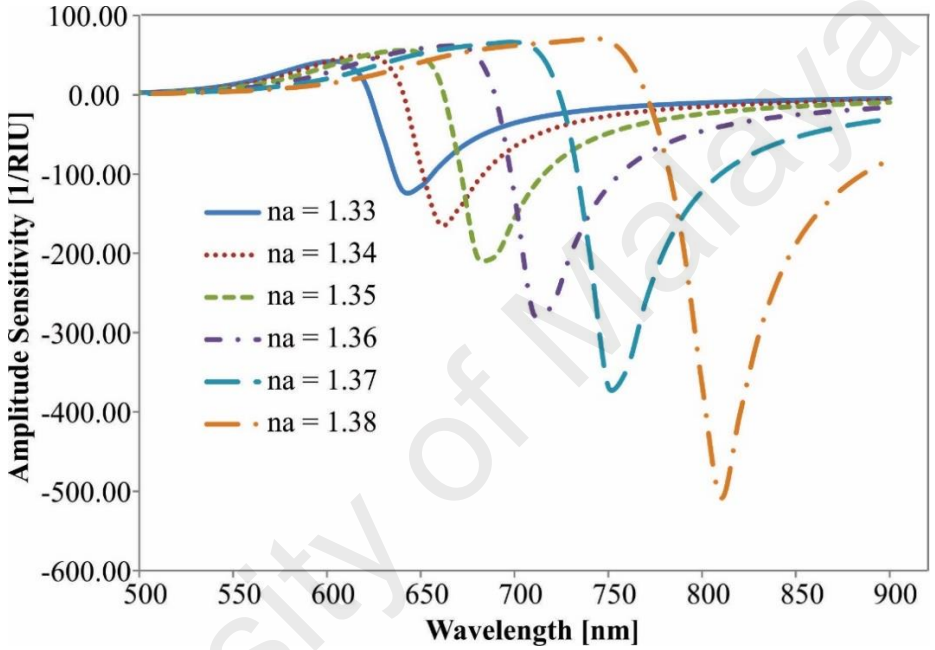

Figure 4.17: Amplitude sensitivity spectrum for different analyte's RI.

From Figure 4.17, the suitable operating wavelength for maximum sensitivity can be determined for a specific refractive index sensing range. For example, for a sensing experiment with the analyte's refractive index from 1.38 to 1.39, the light source with the operating wavelength of 810 nm will be chosen for maximum sensitivity. Amplitude sensitivity of 120, 162, 204, 275 and 368 RIU^{-1} are demonstrated while the analyte RI's are 1.33, 1.34, 1.35, 1.36 and 1.37, respectively. It also shows the maximum sensor resolution of 1.97×10^{-5} RIU (considering amplitude sensitivity of 508 RIU^{-1}) by assuming minimum 1% change of transmitted intensity could be detected accurately.

Sensing performance of the proposed sensor is influenced by the thickness of gold layer because it has significant impact on the surface plasmon wave excitation. Figure 4.18 shows the variation of loss spectrum for analyte RI of 1.33 and 1.34 with varying gold thickness (other parameters are kept constant).

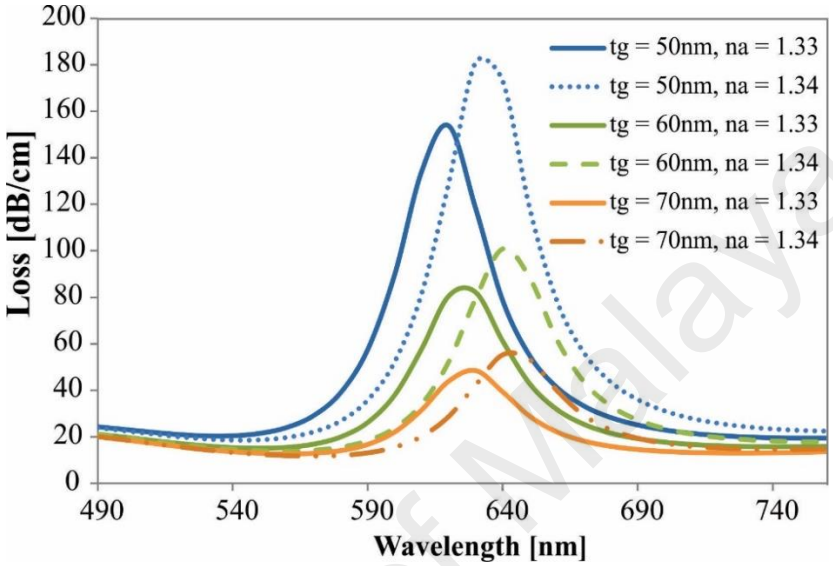

Figure 4.18: Loss spectrums for different gold layer thickness.

Using wavelength interrogation methods, the proposed sensor shows the same sensitivity of 10 nm/RIU at t_g of 50, 60 and 70 nm. However, the phase matching wavelengths are shifted towards the longer values since the effective refractive index of SPP mode bound in gold layer is higher when t_g is increased. Thicker gold layer has more damping loss. Also, the loss depth is decreasing with the increasing of t_g because a thicker gold layer reduces the penetration of core guided mode into cladding. Considering signal-to-noise ratio, the gold thickness is chosen to be 50 nm for the proposed sensor.

4.8 Conclusion

Three DRFs with different waveguide parameters have been fabricated. The concept of fabricating the designed structure using stack-and-draw technique has been proven. From the simulation on the fabricated DRF, DRF with the core size of 0.8 μm provides high evanescent field exposure of 39.56% with two large cavities, 4.2 μm and 10.8 μm

respectively with negligible confinement loss. Suspended-core holey fiber with the same core size can only provide 29% and average cavity size of 3.6 μm. The all-in-one novel DRF has been studied in its contribution to SPR sensing application. As predicted, DRF-based SPR sensor shows maximum wavelength sensitivity of 6000 nm/RIU, which is the highest among all the reported PCF-based SPR sensor.

CHAPTER 5: CONCLUSION AND FUTURE WORK

5.1 Conclusion

Sunny Photonic Crystal Fiber (PCF) has been proposed and numerical analysis shows that sunny structure can boost up the highest achievable sensitivity in a conventional PCF from 7.31% to 10.37% with $d/\Lambda = 0.7$, 10.48% to 13.72% with $d/\Lambda = 0.8$ and 15.83% to 21.23% with $d/\Lambda = 0.9$ with negligible confinement loss. A Sunny PCF with high evanescent field exposure and low confinement loss is a great candidate for sensing application. A preliminary Sunny PCF has also been fabricated by adding an additional step in normal stack-and-draw PCF fabrication process. A novel microstructured optical fiber (MOF) named Diamond Ring Fiber (DRF) has been proposed in this study. DRF can provide large cavities while displaying all the other preferable characteristics as an optical sensor such as enclosed long interaction path, high evanescent field exposed and low confinement loss. Three DRFs with different parameters have been fabricated and tested on their light guiding ability. Numerical analysis shows that DRF with the core size of 0.8 μm (with two cavities measuring 4.2 μm and 10.8 μm) can achieve an evanescent field exposure as high as 39.56% with a negligible confinement loss at a wavelength of 1550 nm. The comparison of the fibers proposed in this thesis with recent literature of evanescent field exposed fibers is summarized in Table 5.1.

Table 5.1: Comparison among evanescent field exposed fibers.

Authors	Evanescent field exposed fibers	Interaction medium	Cavity size	Core size	Evanescent field exposure	Confinement loss
(Birks & Li, 1992)	Tapered fiber	Exposed, short	-	-	-	-
(Lu et al., 2014)	D-shaped fiber	Exposed, short	-	-	-	-
(Monro et al., 2001)	PCF	Enclosed, long	-	-	30% at 1500 nm	313.36 dB/m at 1500 nm
(Fini, 2004)	Defected-core PCF	Enclosed, long	-	-	-	32.4 dB/m at 1500 nm

(Park et al., 2011)	Hollow high index defected-core PCF	Enclosed, long	1.4 µm	-	12.5% at 1500 nm	1.25 dB/m at 1500 nm
(Olyaee & Naraghi, 2013)	Hexagonal high index defected-core PCF	Enclosed, long	-	-	17.5% at 1500 nm	-
(Webb et al., 2007)	Suspended-core holey fiber	Enclosed, long	3.6 µm	0.8 µm	29% at 1550 nm	-
			-	1.2 µm	11.5% at 1550 nm	0.29 dB/m at 1550 nm
(Ng, Rifat, Wong, Tee, et al., 2017)	Sunny PCF	Enclosed, long	-	0.95 µm	29% at 1550 nm	-
			-	1.33 µm	11.5% at 1550 nm	≈ 0 dB/m at 1550 nm
(Ng, Wong, et al., 2017)	DRF	Enclosed, long	4.2 µm 10.8 µm	0.8 µm	39.56% at 1550 nm	< 0.025 dB/m at 1550 nm

DRF has been implemented as a highly sensitive enclosed SPR sensor in RI sensing based on its advantage of having large cavity for gold layer coating and high evanescent field exposure. It demonstrates the maximum wavelength sensitivity of 6000 nm/RIU with the sensor resolution as high as 1.67×10^{-5} RIU. Additionally, maximum amplitude sensitivity is demonstrated to be 508 RIU^{-1} with resolution of 1.97×10^{-5} RIU.

5.2 Future Work

Light-matter interaction is not limited to optical sensing. Fiber laser for example, requires interaction between light and saturable absorber such as graphene nano-particles for achieving passive mode-locking mechanism. Recent work (Lin, Yang, Liou, Yu, & Lin, 2013) has shown that evanescent field mode-locking scheme using PCF effectively enlarges the interaction length of saturable absorption with graphene nano-particles, providing an increasing transmittance and modulation depth. The evanescent wave interaction is found to be better than the traditional approach which confines the graphene nano-particles at the interface of two SMF patchcords. In fact, DRF proposed in this work

is a better candidate in evanescent field mode-locking scheme based on the aforementioned desirable characteristics as an evanescent field exposed structure. Graphene nano-particles can be coated onto the surface in DRF's cavities via siphon phenomenon. Preliminary study has been carry out to find out the method of doing this. The coated DRF has been shown in Figure 5.1.

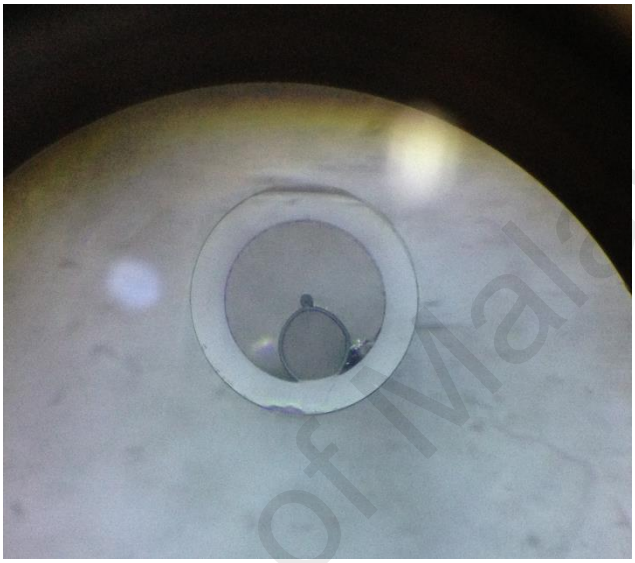

Figure 5.1: Microscope image of a graphene nano-particles coated DRF using siphoning method.

REFERENCES

Agrawal, G. P. (2007). *Nonlinear fiber optics*: Academic press.

Ahmed, R., Rifat, A. A., Yetisen, A. K., Yun, S. H., Khan, S., & Butt, H. (2016). Mode-multiplexed waveguide sensor. *Journal of Electromagnetic Waves and Applications, 30*(4), 444-455.

An, G., Li, S., Yan, X., Zhang, X., Yuan, Z., Wang, H., . . . Han, Z. (2017). Extra-broad photonic crystal fiber refractive index sensor based on surface plasmon resonance. *Plasmonics, 12*(2), 465-471.

Azad, S., Nikzad, A., & Parvizi, R. (2018). Evanescent Field-Modulated Magnetic Immune Sensor Based on Magnetic Fluid and Polymer Optical Fiber. *IEEE Sensors Journal*.

Bariain, C., Matías, I. R., Arregui, F. J., & López-Amo, M. (2000). Optical fiber humidity sensor based on a tapered fiber coated with agarose gel. *Sensors and Actuators B: Chemical, 69*(1), 127-131.

Berenger, J.-P. (1994). A perfectly matched layer for the absorption of electromagnetic waves. *Journal of computational physics, 114*(2), 185-200.

Birks, T. A., & Li, Y. W. (1992). The shape of fiber tapers. *Journal of lightwave technology, 10*(4), 432-438.

Bobb, L. C., Shankar, P., & Krumboltz, H. (1991). Pressure sensor that uses bent biconically tapered single-mode fibers. *Optics letters, 16*(2), 112-114.

Boehm, J., Fran ̧ois, A., Ebendorff-Heidepriem, H., & Monro, T. M. (2011). Chemical deposition of silver for the fabrication of surface plasmon microstructured optical fibre sensors. *Plasmonics, 6*(1), 133-136.

Botten, L. C., McPhedran, R. C., de Sterke, C. M., Nicorovici, N. A., Asatryan, A. A., Smith, G. H., . . . Kuhlmey, B. T. (2005). From multipole methods to photonic crystal device modeling. *Electromagnetic theory and applications for photonic crystals (optical engineering)(ed. Yasumoto K.)*, 47-122.

Chandra, S., Dhawangale, A., & Mukherji, S. (2018). Hand-held optical sensor using denatured antibody coated electro-active polymer for ultra-trace detection of copper in blood serum and environmental samples. *Biosensors and Bioelectronics, 110*, 38-43.

Cheng, D. K. (1989). *Field and wave electromagnetics*: Pearson Education India.

Cordeiro, C. M., Franco, M. A., Chesini, G., Barretto, E. C., Lwin, R., Cruz, C. B., & Large, M. C. (2006). Microstructured-core optical fibre for evanescent sensing applications. *Optics express, 14*(26), 13056-13066.

Dash, J. N., & Jha, R. (2014). SPR biosensor based on polymer PCF coated with conducting metal oxide. *IEEE Photonics Technology Letters, 26*(6), 595-598.

Dash, J. N., & Jha, R. (2015). On the performance of graphene-based D-shaped photonic crystal fibre biosensor using surface plasmon resonance. *Plasmonics, 10*(5), 1123-1131.

Ebendorff-Heidepriem, H., Petropoulos, P., Asimakis, S., Finazzi, V., Moore, R. C., Frampton, K., . . . Monro, T. (2004). Bismuth glass holey fibers with high nonlinearity. *Optics express, 12*(21), 5082-5087.

El Hamzaoui, H., Bigot, L., Bouwmans, G., Razdobreev, I., Bouazaoui, M., & Capoen, B. (2011). From molecular precursors in solution to microstructured optical fiber: a Sol-gel polymeric route. *Optical Materials Express, 1*(2), 234-242.

Euser, T. G., Chen, J., Scharrer, M., Russell, P. S. J., Farrer, N. J., & Sadler, P. (2008). Quantitative broadband chemical sensing in air-suspended solid-core fibers. *Journal of applied physics, 103*(10), 103108.

Ferrarini, D., Vincetti, L., Zoboli, M., Cucinotta, A., & Selleri, S. (2002). Leakage properties of photonic crystal fibers. *Optics express, 10*(23), 1314-1319.

Fini, J. M. (2004). Microstructure fibres for optical sensing in gases and liquids. *Measurement Science and Technology, 15*(6), 1120.

Frazao, O., Santos, J. L., Araújo, F. M., & Ferreira, L. A. (2008). Optical sensing with photonic crystal fibers. *Laser & Photonics Reviews, 2*(6), 449-459.

Furusawa, K. (2003). *Development of rare-earth doped microstructured optical fibres.* University of Southampton.

Gallagher, D. F., & Felici, T. P. (2003). *Eigenmode expansion methods for simulation of optical propagation in photonics: pros and cons.* Paper presented at the Proceedings of SPIE.

Gao, D., Guan, C., Wen, Y., Zhong, X., & Yuan, L. (2014). Multi-hole fiber based surface plasmon resonance sensor operated at near-infrared wavelengths. *Optics Communications, 313*, 94-98.

Hameed, M. F. O., Alrayk, Y. K., Shaalan, A. A., El Deeb, W. S., & Obayya, S. S. (2016). Design of highly sensitive multichannel bimetallic photonic crystal fiber biosensor. *Journal of Nanophotonics, 10*(4), 046016-046016.

Hand, D., & Russell, P. S. J. (1990). Photoinduced refractive-index changes in germanosilicate fibers. *Optics letters, 15*(2), 102-104.

Hansen, T. P., Broeng, J., Jakobsen, C., Vienne, G., Simonsen, H. R., Nielsen, M. D., . . . Bjarklev, A. (2004). Air-guiding photonic bandgap fibers: spectral properties, macrobending loss, and practical handling. *Journal of lightwave technology, 22*(1), 11.

Harun, S., Lim, K., Tio, C., Dimyati, K., & Ahmad, H. (2013). Theoretical analysis and fabrication of tapered fiber. *Optik-International Journal for Light and Electron Optics, 124*(6), 538-543.

Hassani, A., & Skorobogatiy, M. (2006). Design of the microstructured optical fiber-based surface plasmon resonance sensors with enhanced microfluidics. *Optics express, 14*(24), 11616-11621.

Hill, K., Fujii, Y., Johnson, D. C., & Kawasaki, B. (1978). Photosensitivity in optical fiber waveguides: Application to reflection filter fabrication. *Applied physics letters, 32*(10), 647-649.

Homola, J. (2003). Present and future of surface plasmon resonance biosensors. *Analytical and bioanalytical chemistry, 377*(3), 528-539.

Hoo, Y. L., Jin, W., Shi, C., Ho, H. L., Wang, D. N., & Ruan, S. C. (2003). Design and modeling of a photonic crystal fiber gas sensor. *Applied optics, 42*(18), 3509-3515.

Iadicicco, A., Cusano, A., Cutolo, A., Bernini, R., & Giordano, M. (2004). Thinned fiber Bragg gratings as high sensitivity refractive index sensor. *IEEE Photonics Technology Letters, 16*(4), 1149-1151.

Izawa, T., & Sudo, S. (1987). Optical fibers: materials and fabrication. *KTK Scientific Publishers, 1987*, 186.

Johnson, S. G., & Joannopoulos, J. D. (2001). Block-iterative frequency-domain methods for Maxwell's equations in a planewave basis. *Optics express, 8*(3), 173-190.

Jorgenson, R., & Yee, S. (1993). A fiber-optic chemical sensor based on surface plasmon resonance. *Sensors and Actuators B: Chemical, 12*(3), 213-220.

Kaiser, P., Marcatili, E., & Miller, S. (1973). A new optical fiber. *Bell Labs Technical Journal, 52*(2), 265-269.

Kashyap, R. (1994). Photosensitive optical fibers: Devices and applications. *Optical fiber technology, 1*(1), 17-34.

Kenny, R., Birks, T., & Oakley, K. (1991). Control of optical fibre taper shape. *Electronics Letters, 27*(18), 1654-1656.

Kersey, A. D., Davis, M. A., Patrick, H. J., LeBlanc, M., Koo, K., Askins, C., . . . Friebele, E. J. (1997). Fiber grating sensors. *Journal of lightwave technology, 15*(8), 1442-1463.

Kiang, K., Frampton, K., Monro, T., Moore, R., Tucknott, J., Hewak, D., . . . Rutt, H. (2002). Extruded singlemode non-silica glass holey optical fibres. *Electronics Letters, 38*(12), 546-547.

Knight, J., Birks, T., Russell, P. S. J., & Atkin, D. (1996). All-silica single-mode optical fiber with photonic crystal cladding. *Optics letters, 21*(19), 1547-1549.

Knight, J. C. (2003). Photonic crystal fibres. *Nature, 424*(6950), 847.

Koshiba, M. (1992). Optical waveguide theory by the finite element method.

Kumar, V. R. K., George, A., Reeves, W., Knight, J., Russell, P. S. J., Omenetto, F., & Taylor, A. (2002). Extruded soft glass photonic crystal fiber for ultrabroad supercontinuum generation. *Optics express, 10*(25), 1520-1525.

Kurashima, T., Horiguchi, T., & Tateda, M. (1990). Distributed-temperature sensing using stimulated Brillouin scattering in optical silica fibers. *Optics letters, 15*(18), 1038-1040.

Lee, B. (2003). Review of the present status of optical fiber sensors. *Optical fiber technology, 9*(2), 57-79.

Lee, H. W. (2012). Plasmonic photonic crystal fiber.

Li, S.-G., Liu, S.-Y., Song, Z.-Y., Han, Y., Cheng, T.-L., Zhou, G.-Y., & Hou, L.-T. (2007). Study of the sensitivity of gas sensing by use of index-guiding photonic crystal fibers. *Applied optics, 46*(22), 5183-5188.

Li, T. (2012). *Optical fiber communications: fiber fabrication*: Elsevier.

Liedberg, B., Nylander, C., & Lunström, I. (1983). Surface plasmon resonance for gas detection and biosensing. *Sensors and actuators, 4*, 299-304.

Lin, Y.-H., Yang, C.-Y., Liou, J.-H., Yu, C.-P., & Lin, G.-R. (2013). Using graphene nano-particle embedded in photonic crystal fiber for evanescent wave mode-locking of fiber laser. *Optics express, 21*(14), 16763-16776.

Lu, H., Tian, Z., Yu, H., Yang, B., Jing, G., Liao, G., . . . Luo, Y. (2014). Optical fiber with nanostructured cladding of TiO 2 nanoparticles self-assembled onto a side polished fiber and its temperature sensing. *Optics express, 22*(26), 32502-32508.

Ma, L., Hanzawa, N., Tsujikawa, K., Aozasa, S., & Yamamoto, F. (2015). Loss reduction in few-mode photonic crystal fiber by reducing inner surface imperfections in air holes. *Optics express, 23*(10), 13619-13625.

Meltz, G., Morey, W. W., & Glenn, W. (1989). Formation of Bragg gratings in optical fibers by a transverse holographic method. *Optics letters, 14*(15), 823-825.

Mescia, L., & Prudenzano, F. (2013). Advances on optical fiber sensors. *Fibers, 2*(1), 1-23.

Moar, P., Huntington, S., Katsifolis, J., Cahill, L., Roberts, A., & Nugent, K. (1999). Fabrication, modeling, and direct evanescent field measurement of tapered optical fiber sensors. *Journal of applied physics, 85*(7), 3395-3398.

Monro, T. M., Belardi, W., Furusawa, K., Baggett, J. C., Broderick, N., & Richardson, D. (2001). Sensing with microstructured optical fibres. *Measurement Science and Technology, 12*(7), 854.

Monro, T. M., Richardson, D., & Bennett, P. (1999). Developing holey fibres for evanescent field devices. *Electronics Letters, 35*(14), 1188-1189.

Monro, T. M., Warren-Smith, S., Schartner, E. P., Fran ̧ois, A., Heng, S., Ebendorff-Heidepriem, H., & Afshar, S. (2010). Sensing with suspended-core optical fibers. *Optical fiber technology*, *16*(6), 343-356.

Ng, W. L., Rifat, A. A., Wong, W. R., Mahdiraji, G., & Adikan, F. M. (2017). A Novel Diamond Ring Fiber-Based Surface Plasmon Resonance Sensor. *Plasmonics*, 1-6.

Ng, W. L., Rifat, A. A., Wong, W. R., Tee, D. C., & Mahamd Adikan, F. R. (2017). Enhancement of evanescent field exposure in a photonic crystal fibre with interstitial holes. *Journal of Modern Optics*, *64*(15), 1544-1549.

Ng, W. L., Wong, W. R., Mahdiraji, G. A., Rifat, A. A., Tee, D. C., & Adikan, F. R. M. (2017). Diamond ring fiber for evanescent field exposure. *Optics letters*, *42*(8), 1544-1547.

Olyaee, S., & Naraghi, A. (2013). Design and optimization of index-guiding photonic crystal fiber gas sensor. *Photonic Sensors*, *3*(2), 131.

Olyaee, S., Naraghi, A., & Ahmadi, V. (2014). High sensitivity evanescent-field gas sensor based on modified photonic crystal fiber for gas condensate and air pollution monitoring. *Optik-International Journal for Light and Electron Optics*, *125*(1), 596-600.

Otupiri, R., Akowuah, E., Haxha, S., Ademgil, H., AbdelMalek, F., & Aggoun, A. (2014). A novel birefrigent photonic crystal fiber surface plasmon resonance biosensor. *IEEE Photonics Journal*, *6*(4), 1-11.

Park, J., Lee, S., Kim, S., & Oh, K. (2011). Enhancement of chemical sensing capability in a photonic crystal fiber with a hollow high index ring defect at the center. *Optics express*, *19*(3), 1921-1929.

Payne, F. (1989). Photorefractive gratings in single-mode optical fibres. *Electronics Letters*, *25*(8), 498-499.

Poletti, F. (2007). *Direct and inverse design of microstructured optical fibres.* University of Southampton.

Rao, Y., & Zhu, T. (2007). *A highly sensitive fiber-optic refractive index sensor based on an edge-written long-period fiber grating.* Paper presented at the Bragg Gratings, Photosensitivity, and Poling in Glass Waveguides.

Rifat, A., Mahdiraji, G. A., Sua, Y., Shee, Y., Ahmed, R., Chow, D. M., & Adikan, F. M. (2015). Surface plasmon resonance photonic crystal fiber biosensor: a practical sensing approach. *IEEE Photon. Technol. Lett.*, *27*(15), 1628-1631.

Rifat, A. A., Ahmed, R., Mahdiraji, G. A., Adikan, F. M., & Miroshnichenko, A. E. (2018). Highly sensitive selectively coated photonic crystal fiber-based plasmonic sensor. *Optics letters*, *43*(4), 891-894.

Rifat, A. A., Ahmed, R., Yetisen, A. K., Butt, H., Sabouri, A., Mahdiraji, G. A., . . . Adikan, F. M. (2016). Photonic crystal fiber based plasmonic sensors. *Sensors and Actuators B: Chemical*.

Rifat, A. A., Mahdiraji, G. A., Chow, D. M., Shee, Y. G., Ahmed, R., & Adikan, F. R. M. (2015). Photonic crystal fiber-based surface plasmon resonance sensor with selective analyte channels and graphene-silver deposited core. *Sensors, 15*(5), 11499-11510.

Robinson, G. (1995). The commercial development of planar optical biosensors. *Sensors and Actuators B: Chemical, 29*(1-3), 31-36.

Romolini, A., Falciai, R., & Schena, A. (1998). Biconically-tapered optical fiber probes for the measurement of esophageal pressure. *Sensors and Actuators A: Physical, 70*(3), 205-210.

Russell, P. (2003). Photonic crystal fibers. *science, 299*(5605), 358-362.

Sacks, Z. S., Kingsland, D. M., Lee, R., & Lee, J.-F. (1995). A perfectly matched anisotropic absorber for use as an absorbing boundary condition. *IEEE transactions on Antennas and Propagation, 43*(12), 1460-1463.

Saitoh, K., & Koshiba, M. (2001). Full-vectorial finite element beam propagation method with perfectly matched layers for anisotropic optical waveguides. *Journal of lightwave technology, 19*(3), 405.

Saitoh, K., & Koshiba, M. (2003). Confinement losses in air-guiding photonic bandgap fibers. *IEEE Photonics Technology Letters, 15*(2), 236-238.

Sazio, P. J., Amezcua-Correa, A., Finlayson, C. E., Hayes, J. R., Scheidemantel, T. J., Baril, N. F., . . . Margine, E. R. (2006). Microstructured optical fibers as high-pressure microfluidic reactors. *science, 311*(5767), 1583-1586.

Shadaram, M., Espada, L., Martinez, J., & Garcia, F. (1998). Modeling and performance evaluation of ferrocene-based polymer clad tapered optical fiber gas sensors. *Optical Engineering, 37*(4), 1124-1129.

Shuai, B., Xia, L., & Liu, D. (2012). Coexistence of positive and negative refractive index sensitivity in the liquid-core photonic crystal fiber based plasmonic sensor. *Optics express, 20*(23), 25858-25866.

Stewart, G., Jin, W., & Culshaw, B. (1997). Prospects for fibre-optic evanescent-field gas sensors using absorption in the near-infrared. *Sensors and Actuators B: Chemical, 38*(1-3), 42-47.

Stewart, G., Norris, J., Clark, D., & Culshaw, B. (1991). Evanescent-wave chemical sensors--a theoretical evaluation. *International Journal of Optoelectronics, 6*(3), 227-238.

Stone, J. (1987). Photorefractivity in GeO2-doped silica fibers. *Journal of applied physics, 62*(11), 4371-4374.

Sun, L., Jiang, S., & Marciante, J. (2010). All-fiber optical magnetic-field sensor based on Faraday rotation in highly terbium-doped fiber. *Optics express, 18*(6), 5407-5412.

Syms, R. R., & Cozens, J. R. (1992). *Optical guided waves and devices*: McGraw-Hill.

Tatian, B. (1984). Fitting refractive-index data with the Sellmeier dispersion formula. *Applied optics, 23*(24), 4477-4485.

Tian, M., Lu, P., Chen, L., Lv, C., & Liu, D. (2012). All-solid D-shaped photonic fiber sensor based on surface plasmon resonance. *Optics Communications, 285*(6), 1550-1554.

Tong, L., Gattass, R. R., Ashcom, J. B., He, S., Lou, J., Shen, M., . . . Mazur, E. (2003). Subwavelength-diameter silica wires for low-loss optical wave guiding. *Nature, 426*(6968), 816-819.

Tse, M.-L. V. (2007). *Development and applications of dispersion controlled high nonlinearity microstructured fibres.* University of Southampton.

Tubb, A., Payne, F., Millington, R., & Lowe, C. (1995). Single mode optical fibre surface plasma wave chemical sensor.

Udd, E., & Spillman Jr, W. B. (2011). *Fiber optic sensors: an introduction for engineers and scientists*: John Wiley & Sons.

Vial, A., Grimault, A.-S., Macías, D., Barchiesi, D., & de La Chapelle, M. L. (2005). Improved analytical fit of gold dispersion: Application to the modeling of extinction spectra with a finite-difference time-domain method. *Physical Review B, 71*(8), 085416.

Wang, F., Sun, Z., Liu, C., Sun, T., & Chu, P. K. (2016). A highly sensitive dual-core photonic crystal fiber based on a surface plasmon resonance biosensor with silver-graphene layer. *Plasmonics*, 1-7.

Wang, J., Jiang, C., Hu, W., & Gao, M. (2007). Properties of index-guided PCF with air-core. *Optics & Laser Technology, 39*(2), 317-321.

Webb, A. S., Poletti, F., Richardson, D. J., & Sahu, J. K. (2007). Suspended-core holey fiber for evanescent-field sensing. *Optical Engineering, 46*(1), 010503-010503-010503.

White, T., Kuhlmey, B., McPhedran, R., Maystre, D., Renversez, G., De Sterke, C. M., & Botten, L. (2002). Multipole method for microstructured optical fibers. I. Formulation. *JOSA B, 19*(10), 2322-2330.

Wilson, J., & Hawkes, J. F. B. (1998). *Optoelectronics: an introduction*: Prentice Hall Europe.

Wong, W. R., Krupin, O., Sekaran, S. D., Mahamd Adikan, F. R., & Berini, P. (2014). Serological diagnosis of dengue infection in blood plasma using long-range surface plasmon waveguides. *Analytical chemistry, 86*(3), 1735-1743.

Yajima, T., Yamamoto, J., Ishii, F., Hirooka, T., Yoshida, M., & Nakazawa, M. (2013). Low-loss photonic crystal fiber fabricated by a slurry casting method. *Optics express, 21*(25), 30500-30506.

Yu, X., Sun, Y., Ren, G., Shum, P., Ngo, N., & Kwok, Y. (2008). Evanescent field absorption sensor using a pure-silica defected-core photonic crystal fiber. *IEEE Photonics Technology Letters, 20*(5), 336-338.

Zhang, T., Ma, L., Bai, H., Tong, C., Dai, Q., Kang, C., & Yuan, L. (2014). Design and fabrication of a novel core-suspended optic fiber for distributed gas sensor. *Photonic Sensors, 4*(2), 97.

Zhao, Y., Cai, L., Li, X.-G., Meng, F.-c., & Zhao, Z. (2014). Investigation of the high sensitivity RI sensor based on SMS fiber structure. *Sensors and Actuators A: Physical, 205*, 186-190.

Zhao, Y., Li, X.-g., Cai, L., & Yang, Y. (2015). Refractive index sensing based on photonic crystal fiber interferometer structure with up-tapered joints. *Sensors and Actuators B: Chemical, 221*, 406-410.

Zhi-guo, Z., Fang-di, Z., Min, Z., & Pei-da, Y. (2008). Gas sensing properties of index-guided PCF with air-core. *Optics & Laser Technology, 40*(1), 167-174.

LIST OF PUBLICATIONS AND PAPERS PRESENTED

1. **Ng, W. L.**, Tee, D. C., Yeo, K. S., Mahdiraji, G. A., Lin, G. R., & Adikan, F. R. M. (2015, October). Enhancement of Exposed Evanescent Field in a Photonic Crystal Fiber with Triangular Air Holes around the Core for Chemical Sensing. In Frontiers in Optics (pp. FTh4E-5). Optical Society of America.
2. **Ng, W. L.**, Rifat, A. A., Wong, W. R., Tee, D. C., & Mahamd Adikan, F. R. (2017). Enhancement of evanescent field exposure in a photonic crystal fibre with interstitial holes. Journal of Modern Optics, 64(15), 1544-1549.
3. **Ng, W. L.**, Wong, W. R., Mahdiraji, G. A., Rifat, A. A., Tee, D. C., & Adikan, F. R. M. (2017). Diamond ring fiber for evanescent field exposure. Optics Letters, 42(8), 1544-1547.
4. **Ng, W. L.**, Rifat, A. A., Wong, W. R., Mahdiraji, G. A., & Adikan, F. M. (2017). A Novel Diamond Ring Fiber-Based Surface Plasmon Resonance Sensor. Plasmonics, 1-6.